ISBN 978-2-910015-81-7

NOTES SCIENTIFIQUES ET TECHNIQUES
DE L'INSTITUT DE MÉCANIQUE CÉLESTE

S109

INPOP19a planetary ephemerides

A. Fienga, P. Deram, V. Viswanathan, A. Di Ruscio, L. Bernus, D. Durante, M. Gastineau, and J. Laskar

IMCCE éditions
Institut de Mécanique Céleste et de Calcul des Éphémérides

Institut de mécanique céleste et de calcul des éphémérides
CNRS UMR 8028 / Observatoire de Paris
77, avenue Denfert-Rochereau
75014 Paris

14 Décembre 2019

Abstract

INPOP19a is the new ephemerides for the orbits of the 8 planets of the solar system, the moon, Pluto as well as 14000 asteroids. It is fitted over about 155000 planetary observations including 9 positions of Jupiter deduced from the Juno mission, an extension of the Cassini data sample from 2014 to 2017 for the Saturn orbit and of the MEX data from 2016.4 to 2017.4 for the Mars orbit. The asteroid orbits were fitted on the almost 2 millions of observations obtained by the GAIA mission and delivered with the DR2. The INPOP dynamical modelling was also modified in comparison to the previous version, INPOP17a. A ring modeling the accelerations induced by Trans-Neptunian objects as well as the 9 most massive TNOs have been added in order to improve the fit to the Saturn observations. A new estimation of the TNO ring mass has been produced. Finally a new bayesian procedure for the computation of the masses of 343 main-belt asteroids has been applied and leads to an important improvement in the accuracy of the Mars orbit and of its extrapolation capabilities.

1 Introduction

In this new ephemerides, the nine first perijove of Juno around Jupiter have been included improving the uncertainty of the Jupiter barycentric orbit. Furthermore with the end of the Cassini mission in 2017, a new analysis of the data used for the navigation and for the radio experiment was proposed in order to benefit from the best knowledge in terms of gravity fields and Cassini orbital systematics accumulated over the mission duration. In this context, new positions deduced from an independent analysis of Cassini data were obtained and taken into account into the INPOP construction, expending the time coverage for the Cassini data sample from 2004 to 2017. The section 2 will give a description of the Cassini and Juno analysis. In [3], a new bayesian method for the estimation of the asteroid masses was introduced leading to the determination of 343 asteroid masses constrained by the spectroscopic complex. A supplementary set of trans-neptunian objects with fixed masses have also been added in the modeling as well as a circular ring enclosed by two Neptune resonances at 39.7 and 44 AU.The mass of this ring is estimated during the INPOP adjustment. Besides the INPOP19a construction, a fit of 14000 asteroid orbits integrated together with the planetary orbits has been performed in using the GAIA DR2.

2 Update of the INPOP data sample

The full dataset used for the INPOP19a adjustment is presented in Tab 1.In this table are given the periods of each data sample as well as the number of observations and their average accuracies. The last two columns give the weighted root mean square (WRMS) for each data sample estimated with INPOP19a and INPOP17a.

2.1 Cassini independent data analysis

Refined Cassini's normal points have been produced from a re-analysis of navigation data for the periods 2006, 2008-2009 and 2011. The new data analysis relies on the updated knowledge of the Saturnian system acquired throughout the mission: the enhanced accuracies achieved for Saturn's moons ephemerides and the last gravity solutions of Saturn and its major satellites produced by the radio science team. The analysis shares the same concept of the navigation team's reconstruction setup: trajectory arcs of approximately one month, spanning between two consecutive moons flybys (mainly Titan). For each arc we solve for the spacecraft initial position and velocity, corrections to orbital trim and reaction wheel desaturation maneuvers and RTG-induced anisotropic acceleration. In addition, stochastic accelerations at the level of 5×10^{-13} km/s^2 (updated every 8 hours) are included to compensate for any remaining dynamical mismodeling. Considering the very good accuracy

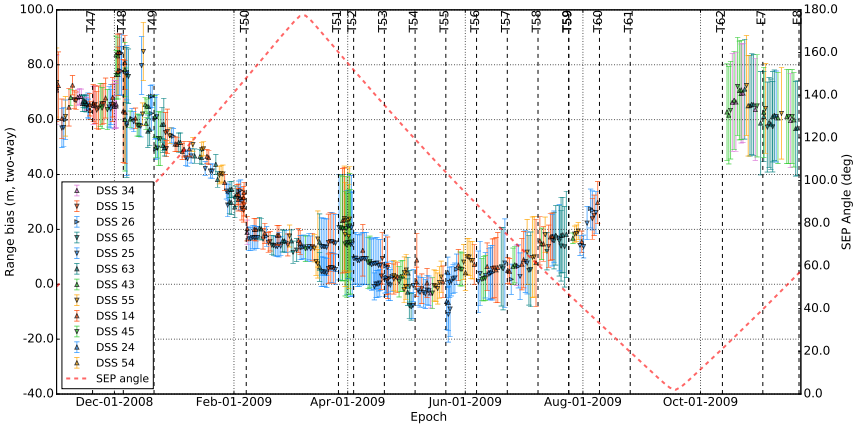

Figure 1: Estimated two-way range biases and formal uncertainties for the period 2008-2009. The annual trend is due to the residual error of INPOP17a ephemerides in the Earth-Saturn barycenter relative positioning.

obtained by [2] and [11] for the Titan and Saturn gravity fields, these latest were not adjusted in our analysis The dataset consists of two-way X-band Doppler and range data. We estimate correction to range measurements in the form of stochastic biases, different for each tracking pass, with large *a priori* uncertainty to absorb both station calibration and ephemerides error. In Fig **??** are plotted the two-way range bias estimated over the period 2008:2009. The error bars were obtained by the projection of the least square covariance matrix on the line of sight.
The reconstructed Cassini trajectories are thus used to produce normal points, including the estimated range biases in the ground station-Cassini round-trip light-time computation. The uncertainty on the normal points is given be the estimated covariance matrix of range biases.
We have added also additional normal points deduced from the radio science solutions for the gravity-dedicated Titan flybys and Grand Finale Saturn pericenters. These range normal points were obtained in considering given spacecraft orbits constrained with only Doppler data for the Titan and Saturn gravity field estimations. By considering these supplementary normal points the period covered by the Cassini has been extended up to the end of 2017. In Tab. 1, the newly analysed normal points and the normal points deduced from Titan gravity flybys are labelled *La Sapienza range* when the data set deduced from the Grand Finale is labelled *Grand Finale range*.

2.2 Nine perijove of Juno

The Juno spacecraft is currently orbiting Jupiter in a highly eccentric, polar orbit since 2016. A radio-science experiment aims at characterizing the gravity field of the gas giant to unprecedented accuracy [6], [10]. Juno extremely accurate radio tracking system enables simultaneous two-way Doppler measurements at X- and Ka-band during the gravity-dedicated passes, which are used to reconstruct the spacecraft trajectory with mHz accuracies in the radial direction, at perijove. Range data points at X-band are collected as well, and Jovian barycenter positions relative to the Earth can be generated once per perijove pass, provided that we know Juno position with respect to the Jovian barycenter. In our fit, we include a total of 9 new Jupiter normal points spanning period from the orbital insertion, back in 2016, to end 2018.

3 Asteroid mass determination

As described in [3], we combine knowledge of the physical properties of asteroids by spatial or ground-based surveys, in particular spectral classes, to planetary ephemerides determinations of masses in order to enlarge the set of estimated asteroid masses and study their consistency with the spectral classes of the asteroids. For the mass determination, we use a constrained least square method based on the BVLS (Bounded Values Least Squares) algorithm from [13] which limits the fitted parameters to given intervals. Bounds have been selected according to the parameters of the fit: for asteroid masses, the lower bounds and the upper bounds are chosen according to the *a priori* masses and the *a priori* uncertainties deduced from the literature. The selection of 343 asteroids perturbing the planetary orbits is done based on the method of [12] and [7]. For defining the bounds, we separate the sample in the three taxonomic complexes C, S, and X according to the spectral informations extracted from the M3PC data base (mp3c.oca.eu). The spectra classes of asteroids can be grouped into the C-, S-, and X-complexes. For each asteroid, we estimate the smallest (lower bound) and the highest (upper bound) densities acceptable for these objects according to given uncertainties. The distribution of the lower bounds and of the upper bounds will constitute the prior distribution of the densities. In order to use the prior knowledge of the spectral complexes but in avoiding too strong constraints in the fit, we consider for each complex gaussian distributions of densities. Lower bounds values have been randomly selected in a (mean - 1σ) gaussian distribution when the upper bounds have been randomly selected in a (mean + 1σ) gaussian distribution. We then translate the density bounds into mass bounds as $\frac{4}{3}\pi D^3 \rho_{\text{guess}}$, i.e. assuming that the quoted D-values are spherical equivalent diameters.

A priori uncertainties on the initial guess values for the masses are also deduced by including the $3-\sigma$ diameter uncertainties to the density lower bounds and the upper bounds. A detailed description of the method is given in [3]. For each Monte Carlo runs, an iterative fit is performed in using the full planetary data sample (see Table 1). INPOP19a was selected among about 3600 adjustments, including the masses of the 343 perturber asteroids, performed for this study as the one minimizing the postfit residuals. Tab. 3 gives the fitted masses of the 343 asteroids.

4 Trans-Neptunian Objects

In addition to the Main Belt objects described above (see section 3), the ten most massive TNO objects have been added to the list of planetary perturbers. As well as the Main Belt asteroids, their orbits are integrated together with the planets. A ring representing the average influence of TNO enclosed in the two main resonances with Neptune has been modeled in INPOP19a in considering 3 rings introduced by using point-mass bodies spread over three circular orbits located at 39.4, 44 and 47.5 AU. The sum of the mass of these three rings is estimated during the INPOP adjustment together with other parameters.. With the INPOP19a data sample including Juno and Cassini updated samples, we obtain for the TNO ring a mass of

$$M_{ring} = (0.061 \pm 0.001) M_E.$$

If we limit the data sample to the sample used by [17], we obtain a mass of

$$M_{ring} = (0.020 \pm 0.003) M_E$$

consistent at 2-σ with the mass obtained by [17], considering the fact that the masses of the major TNO objects included in the modele are fixed in INPOP when they are fitted in [17]. So it is reasonable to think that the uncertainties of the fixed TNO masses in INPOP have been absorbed by the TNO ring mass, inducing a slightly bigger mass than the one obtained by [17]. We fixed the

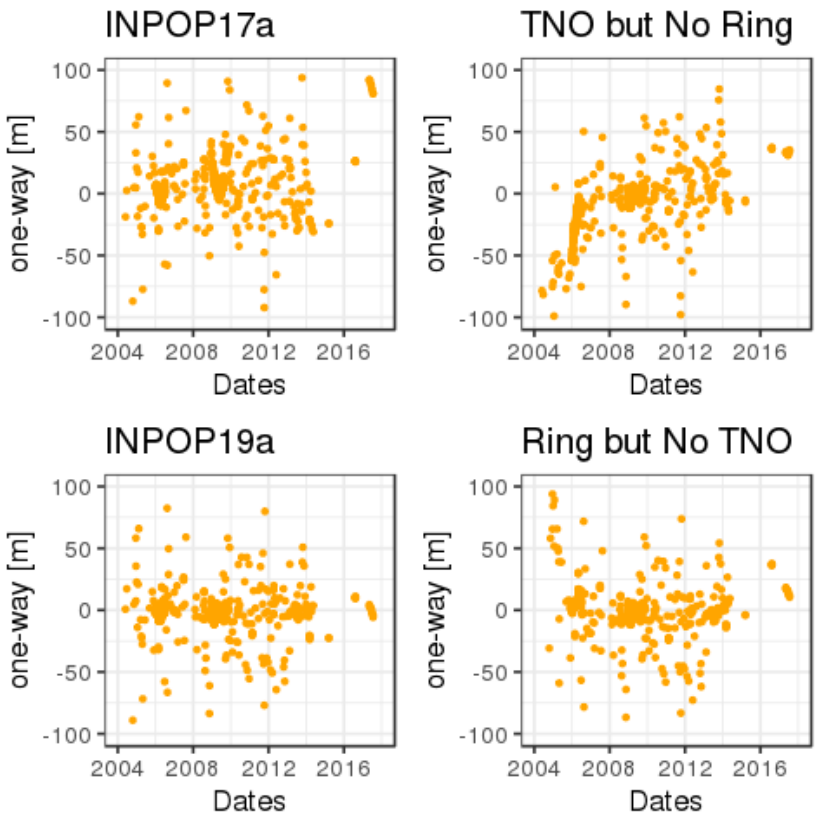

Figure 2: Saturn Postfit residuals obtained with INPOP17a (no ring, no TNO), INPOP19a (ring and TNO), one ephemeris including individual TNOs but no Ring (TNO but No Ring) and one ephemeris including a TNO ring but no individual TNOs (Ring but No TNO).

masses for the ten more massives TNO because these objects have at least one satellite and their masses are very accurately measured by the study of their satellites orbits (see Tab. 2).

The impact of the new modeling is clearly visible on the plots shown on Figure 2. On these plots, one can see the Saturn postfit residuals deduced from the Cassini mission obtained with INPOP17a (with no ring and no individual TNOs) and with 3 differents modeles: one without individual TNO and TNO ring, one with individual TNO but no ring, one with both ring and individual TNO (INPOP19a). It appears clearly that the combined use of the 9 most massive TNOs together with the adjustment of the mass of a TNO ring improves significantly the postfit residuals, in particular if one considers an interval of time spread over several decades. With INPOP17a, the TNO accelerations were not required as the time span of the Cassini data was limited over almost 10 years (from 2004 to 2014). With the Grand Finale, the data sample has been extended over 13 years and INPOP17a clearly shows some trends (including bias) for the latest period (2017) that are not present when we include the full modeling including TNO individuals and ring .

5 INPOP accuracy

The global parameters of the INPOP19a ephemerides can be found in Tab. 3. This table is completed with the one (Tab. 10) of the 343 asteroids masses.

5.1 Postfit residuals

The last two columns of Table 1 give the WRMS of the post-residuals obtained for INPOP19a and INPOP17a. As it can be seen the improvement is clear for Jupiter, Saturn and Mars.

For Mars, as explained in section 3 and in [3], the gain in postfit residuals is significant, in particular for the MRO/MO residuals which are the most accurate available data. In this case, INPOP19a improves INPOP17a residuals by 44% on a common interval of fit. For MEX, the extrapolation of INPOP17a out from its fitting interval (up to 2016.37) explains the more important dispersion of the residuals. However, even on its fitting interval, INPOP17a is less accurate than INPOP19a by 25 %.

For Jupiter the improvement is obviously brought by the Juno tracking data. It reaches 2 order of magnitude: from about 2 km for INPOP17a to 20 m for INPOP19a in keeping good residuals for the other flybys obtained between 1975 to 2001.

For Saturn, the prolongation of the data set from 2014 to 2017 was crucial to identify the contribution of TNOs into the perturbations to be applied on the Saturn orbit (see section 4). Furthermore the introduction of data obtained between 2006 and 2016 and analyzed independently from JPL (see section 2) is also very important to confirm that these data obtained in between 2006 and 2007 have to be taken into account in the adjustment with a high level of weighting. The improvement between INPOP17a and INPOP19a is of a factor 30 for the Grand Finale and 2.6 for the period between 2006 and 2016.

5.2 Propagation of the INPOP uncertainty

An interesting tool, especially for simulating future space missions, is to propagate with time the uncertainty obtained at J2000.

5.2.1 Mathematical formulation

INPOP is computed by solving numerically equations of motion. Let $X(t)$ be the state vector in barycentric coordinates containing positions and velocities of each body which trajectory is computed. The numerical integrator solves a Cauchy-Lipschitz equations of motion system

$$\frac{\mathrm{d}X}{\mathrm{d}t} = F(X;P), \quad X(t = J2000) = X_0 \tag{1}$$

where $P \in \mathrm{R}^p$ contains all the constant parameters of the ephemeris (initial conditions for the planetary orbits, masses of the sun and of the asteroids including trans-Neptunian objects, oblateness of the sun, earth-moon mass ratio). Let us note that X and P are not independent variables because P includes the initial condition X_0. Modification of P may modify $X(t)$. From this ephemeris, we compute observational simulations in order to compare them to real data. Let $C(t_i, P)$ be the observation at date t_i computed with parameters P (we consider in what follows that the dependence with respect to $X(t_i)$ is included in the dependence with respect to the initial conditions included in P which are integrated by INPOP). The goal of the ephemeris is to minimize some norm of the residuals vector

$$R(t_i, P) = (C(t_i, P) - O(t_i)) \tag{2}$$

where $O(t_i)$ is the real observation at date t_i (for any matrix A, transpose of matrix A is noted ${}^tA$). Usually, and this is what we do here, the linear Gaussian approximation is assumed and it is well known that the parameter s P which minimize $\chi^2 = {}^tRWR$ where W is the weigh matrix representing the observational data accuracy, is given by the algorithm which increments P by iterations by adding

$$\delta P = -({}^tJ_C W J_C)^{-1}\ {}^tJW\ R \tag{3}$$

until convergence is reached. Here, J_C represents the Jacobian matrix of $R(t_i, P)$ or $C(t_i, P)$, which is computed numerically as follows

$$J_C[i;k] = \frac{1}{2\delta_k}\left[C(t_i, P_1, \ldots, P_k + \delta_k, \ldots, P_p) - C(t_i, P_1, \ldots, P_k - \delta_k, \ldots, P_p)\right] \tag{4}$$

Then it is well known that the covariance of P, which represents its uncertainty if the Gaussian and linear approximation are realized, is

$$cov\ P = ({}^tJWJ)^{-1} \tag{5}$$

From here, it is possible to propagate linearly the covariance of any variable computed with respect to the ephemeris and its parameters. Let $H(t, P) \in \mathrm{R}^h$ such a variable. Then for a linear random Gaussian variation of P characterised by a covariance matrix $covP$, we can get the covariance of H at date t

$$cov\ H(t, P) = J_H(t)\ covP\ {}^tJ_H(t) \tag{6}$$

where $J_H(t)$ is the Jacobian matrix of H with respect to P at date t. To compute such a matrix, one needs to do the same procedure as for $C(t_i, P)$ which is formally equivalent.

In what follows, we will compute the linear covariance propagation of planetary RTN geocentric coordinates[1] which are defined according to the following orthonormal basis for any planet A

$$\boldsymbol{u}_A = \frac{\boldsymbol{x}_A - \boldsymbol{x}_{EMB}}{|\boldsymbol{x}_A - \boldsymbol{x}_{EMB}|}, \tag{7}$$

$$\boldsymbol{w}_A = \frac{\boldsymbol{u}_A \times (\boldsymbol{v}_A - \boldsymbol{v}_{EMB})}{|\boldsymbol{u}_A \times (\boldsymbol{v}_A - \boldsymbol{v}_{EMB})|}, \tag{8}$$

$$\boldsymbol{v}_A = \boldsymbol{w}_A \times \boldsymbol{u}_A \tag{9}$$

where $\boldsymbol{x}_A$ and represents the barycentric coordinates of body A, $\boldsymbol{v}_A = \mathrm{d}\boldsymbol{x}_A/\mathrm{d}t$, EMB label represents Earth-Moon barycenter, and $\times$ represents the vectorial product. Then we compute the quantities R_A, T_A, N_A as follows

$$R_A = (\boldsymbol{x}_A - \boldsymbol{x}_{EMB}) \cdot \boldsymbol{u}_A \tag{10}$$

$$T_A = (\boldsymbol{x}_A - \boldsymbol{x}_{EMB}) \cdot \boldsymbol{v}_A \tag{11}$$

$$N_A = (\boldsymbol{x}_A - \boldsymbol{x}_{EMB}) \cdot \boldsymbol{w}_A \tag{12}$$

From here we can deduce the propagated covariance of these three components on different bodies.

It is interesting to compare the evolution of RTN components between two ephemerides. We can compare the difference between the components and the evolution of the covariance for two set of parameters P_1 and P_2 in order to compute a distance between two ephemerides. We can also do this for two different models, like INPOP17a and INPOP19a, in order to see if the difference between both is contained into the uncertainty "tube" of the propagated covariance.

[1] Rigorously we should call it "RTN Earh-Moon-barycenter coordinates" but no confusion is possible with the following definitions.

5.2.2 Application to INPOP and results

From Figures 6 to 12 are presented the propagations of the standard dispersion[2] obtained at the end of the least square adjustment for INPOP19a and INPOP17a in RTN geocentric directions for the planets from Mercury to Neptune as well as the differences between the 2 ephemerides in geocentric RTN. The Figure 13 gives the propagation of the standard dispersion for the EMB orbit relative to the solar system barycenter (given in RTN barycentric). All propagation are given for a 40 years period, from 1980 to 2020.

In all the cases, INPOP19a shows lower propagated standard dispersion in comparison to INPOP17a in all directions and even after 20 years of integration. For Mercury and Venus, the improvement is about a factor 10 when it is of about a factor at least 4 (in R direction) and up to a factor 12 (in N direction) for Mars. For Jupiter, the improvement reaches a factor 50 in R and T directions when for Saturn as well as for Uranus and Neptune, the propagation of the INPOP19a standard dispersion is only 10 times better than the INPOP17a one. The differences between the ephemerides are consistent with the INPOP17a standard dispersion for the inner planets but are significantly greater for the outer planets. This can be explained by the introduction of the TNO in INPOP19a. As their contributions are mostly significant for the outer planet orbits and they were not considered in the INPO17a modeling, it is not surprising to have an underestimated uncertainty for INPOP17a for the outer planets. Finally for the EMB, the previous comments are also valid. However one can also note the important differences of the EMB orbit between INPOP19a and INPOP17a. These differences are explained at 97% by the contribution of the individual TNO and by 3% by the increase of 50% of the amount of main-belt asteroids (343 in INPOP19a compared to the 168 in INPOP17a) taken into account in the modelling. These massive bodies orbiting on non-perfectly circular orbits induce a displacement of the solar system barycenter that is visible in the differences of the EMB positions around the SSB between INPOP19a and INPOP17a. Finally it has to be stressed that these standard dispersion propagations are based on covariance matrices directly extracted from the least square adjustment. They give a good representation of the improvement between INPOP17a and INPOP19a. For more a realistic study of the INPOP19a uncertainties, other statistical tests have to be done.

5.3 Extrapolation Tests

Finally, 18 months of MEX data has been put beside in order to test the INPOP19a extrapolation capabilities. On Figure 3 are presented the residuals obtained for INPOP19a and INPOP17a. INPOP17a was fitted up to 2016.7 when INPOP19a was fitted on data up to 2017.37. Let us note the supplementary data interval used for the INPOP19a construction has an important gap, visible on Figure 3, due to the 2017 solar conjunction, leading to an effective supplementary interval of about 5 months. Nevertheless as one can see on Figure 3, the INPOP19a residuals are less important the one obtained with INPOP17a. Over the same interval of extrapolation (18 months), the INPOP19a residual dispersion decreases of about 50% in comparison to INPOP17a. If one considers the full interval, the extrapolation residuals are about about 3 times smaller for INPOP19a than for INPOP17a. This result shows the improvement of INPOP19a relative to INPOP17a in terms of Mars orbit extrapolation.

[2]The propagated standard dispersion is the square root of the propagated variance as defined above.

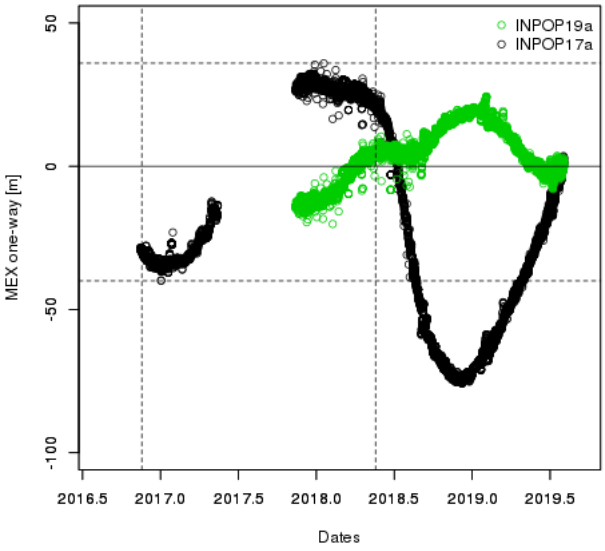

Figure 3: MEX one-way range extrapolation residuals (given in meters) obtained with INPOP17a (black) and INPOP19a (green). These residuals were obtained by comparisons between the ephemerides and observed distances not included in the data sample used for the fit. The dashed vertical lines indicate a 18-month period of extrapolation for INPOP17a and the dashed horizontal lines give the maximum and the minimum of the INPOP17a residuals for this 18-month extrapolation period.

6 Adjustment of asteroid orbit using GAIA DR2

6.1 Method

In 2013, was launched the astrometric satellite GAIA. Among observations of about 1 billion of stars with an accuracy down to 24 μarcseconds, the satellite also observed objects in the solar system. In 2018, were released positions and velocities of about 14 099 known Solar System objects mainly main belt, near Earth and Kuiper belt asteroids based on nearly 2 millions observations. The positions were acquired in the GAIA specific coordinates AL and AC as described in [9] with an optimal range of brightness G=12-17 where the accuracy in the AL-direction reaches milliarcsecond. As the error on AC remains considerably larger, the information provided by GAIA is essentially 1D. These particular features give rise to very strong correlations between right ascension and declination coordinates expressed in the barycentric reference system (BCRS) and have to be fully taken into account during the orbit determination process.

14099 orbits have then been integrated with INPOP together with the planetary and moon orbits. We fit these orbits to the GAIA data in using the correlation matrix provided by the DPAC. We did not fit the planetary orbits together with the asteroid orbits but we iterate the procedure in order to include the asteroid orbital improvements brought by the GAIA observations to the computation and the adjustment of the planet orbits (Mars mainly).

In order to integrate the motion of 14099 orbits in a reasonable time, we included the perturbations of the Sun and of the main planets but in a newtonian formalism and in taking into account only a reduced number of the biggest asteroids that can have an influence on the other asteroid orbits. For a sake of comparison, we chose the same list of perturbing asteroids (16) as in [9]. However, after testing different alternative lists of perturbers, due to the limited interval of time covered by the GAIA data (22 months), no difference are noticeable on the residuals after the fit.

For operating the inversion of such system (The size of the Jacobian matrix is 14099×6 × 1977702×2), a direct adjustment is very time consuming, This is why a strategy of block-wise algorithm has been set up using the Schur complement.

6.2 Asteroid orbit accuracy after fit

Fig. 4 presents the residuals obtained before and after the fit of the 14099 asteroids in using INPOP19a. The obtained results are very similar to those published to [9]. The mean and the standard deviation of the residuals after the adjustment is respectively 0.08 and 2.13 milliarcsecond in AL direction (compared to 0.05 and 2.14 in [9]). 96% of the AL residuals fall in the interval [-5,5] and 53% are at sub-milliarcsecond level. 98% of the AC residuals fall in the interval [-800 800].

6.3 INPOP to Gaia reference frame tie

Because of the addition of 9 TNOs objects in INPOP19a, the position of the solar system barycenter has moved between INPOP19a and the ephemerides used for the definition of the GAIA SSB, INPOP10e [4]. This can lead to a biased estimation of the GAIA spacecraft positions and consequently the asteroid observations. In order to take this offset into account, a constant translation on the GAIA barycentric position at J2000 (epoch of integration of the INPOP ephemerides) was fitted in the same time than asteroid orbit. The obtained value for the vector is x=-86.6, y=-49.3,z=-5.0 km. One can check that an equivalent displacement is obtained when comparing the barycentric EMB positions with respect to the solar system barycenter between INPOP17a (without TNO such as

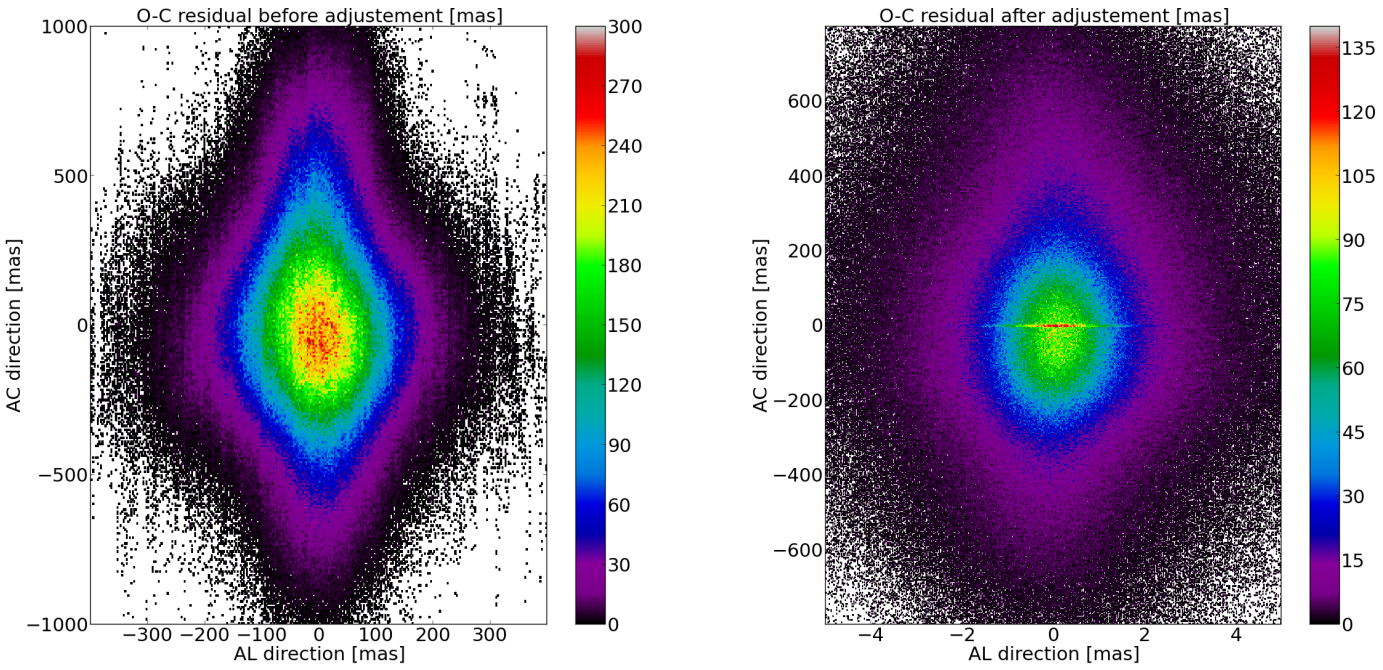

Figure 4: Density plot of the residuals in the (AL,AC) plane expressed in milliarcsecond before and after the adjustement of the initial conditions. The colorbar and the axis range were chosen to be directly comparable with Fig.19 of [9]

INPOP10e) and INPOP19a.

In order to estimate the impact on the INPOP reference frame orientations of the use of the DR2 GAIA fitted asteroid orbits on the planet ones, we estimate a matrix of rotation between two planetary ephemerides differing only by the initial conditions of the orbits of the 343 asteroids taking into account for their perturbations on the planetary orbits.

The two ephemerides were fitted over the same data sample given in Table 1 and in considering the same adjusted parameters. Same residuals have been obtained for the two solutions and no significant differences have been noticed in the fitted parameters, implying that the differences in the asteroid orbits are directly absorbed by the fitted parameters inside the estimated uncertainties.

This choice of fitting a rotation matrix between the two planetary ephemerides can be explained by the fact that the new asteroid orbits fitted over the Gaia DR2 are directly given in the Gaia reference frame ([8]) when the former asteroid orbits were given in a frame close to the one defined with the stellar catalogs such as USNOB1.1 and UCAC, leading to a tie to the ICRF2 with an accuracy of about several hundred of milli-arcseconds (mas) ([1]). This latest frame being at least two order of magnitude less accurate that the other data used for the planetary ephemerides tie to ICRF, when the two ephemerides are compared, we evaluate the rotation between the planetary orbits tied to ICRF with (delta DOR) observations of spacecraft orbiting planets ([5]) and planetary orbits adjusted using both ICRF VLBI positions of spacecraft and asteroid orbits given in the GRF. 3 Euler angles have been fitted and are given in Table 4 for different cases, depending which planetary orbits are considered. If all the orbits including the outer planet ones are considered, the mis-alignement of the INPOP reference frame axis (by definition, the ICRF , without considering the VLBI observation uncertainties) with the Gaia reference frame (GRF) is not significant. However if we consider only the orbits fitted over very accurate observations such as the inner planets, Jupiter and Saturn, then the Euler angles turn out to be significant but at the level of few μas. This is far below the uncertainty of the alignement between DR2 GRF and ICRF3 of about 20 to 30 μas as obtained by ([8]). We can then conclude to a good alignement of the INPOP reference axis relative to the DR2 GRF.

7 Lunar ephemeris

The lunar ephemeris of INPOP19a are obtained from the fit of the integrated solutions of the lunar orbit and orientation to the lunar laser ranging (LLR) data. The LLR data used for the fits of INPOP19a contains 27,780 normal points collected by eight Earth stations ranging to five lunar surface retroreflectors from August 1969 until October 2019. The LLR data is processed using the GINS software and the LLR reduction model is detailed in [22]. The dynamical model of the lunar interior is developed within INPOP19a following the description within [14, 22]. Minor adjustments to the LLR data weights is made to benefit from the high accuracy of the LLR observations from APOLLO and Grasse stations. A total of 5725 infrared LLR observations collected between 2015-2019 were used for the fits of INPOP19a. The LLR data from the Wetzell station were retrieved from the POLAC and ILRS FTP websites for 2018 and 2019 data respectively. The comparison of LLR post-fit wrms obtained with INPOP17a and INPOP19a are provided in Table 5. We find that the wrms of the INPOP19a LLR post-fit residuals are very close to the 1 cm mark for Grasse, APOLLO and Wettzell stations.

The LLR fits of INPOP19a includes a supplementary correction to the longitude libration of the Moon (introduced within the GINS reduction software) to account for frequency dependence of lunar tidal dissipation. This introduces 3 cosine terms (l', 2l-2D, 2F-2l) as corrections to the longitude libration of the Moon, similar to DE430 [25] and following the approximation in EPM2016 [15]. The cosine terms provide the out-of-phase component to the sine-dominated longitude libration terms (see for example the Fourier terms in the physical libration for τ tabulated in [18]). Introducing these

terms improves the LLR post-fit residuals by few mm (3-4 mm) visible more prominently over years 2010 to 2019, due to the higher accuracy of LLR data acquired during this period. The annual term (l') has the most prominence among the three fitted amplitudes. Their values are tabulated in Table 7. We adapt this method for providing users with high accuracy requirements, until an equivalent dynamical model representation is introduced. Amplitudes of terms with longer periods ($\geq$ 3yr) could in principle be fit at the current accuracy and long baseline of the data, but does not contribute to a significant improvement in the post-fit residuals.

Some of the parameters relevant to the Earth-Moon system are tabulated in Table 6. The differences in the gravitational mass of the Earth-Moon barycentre (GM_{EMB}) arise from the use of updated values of the Earth-Moon mass ratio (EMRAT) provided by the joint iterative fit to the planetary part of the ephemeris. The INPOP17a solution reported a mean radial difference of $\sim$ 19 cm with respect to the last update of the JPL lunar solution (DE430) arising from the differences in GM_{EMB} [22]. This difference is now reduced to $\sim$ 5 cm with the INPOP19a solution. Other differences in the lunar interior parameters are within their respective error bars. Few of the lunar gravity field coefficients (tabulated in Table 6) continue to require adjustment outside the error bar provided by the GRAIL gravity field solutions for a better fit of the LLR data. This is likely due to the simplicity of the forward modeling of the interior dynamics of the Moon as shown through recent efforts involving the joint analysis of GRAIL-LLR solutions [23]. The fluid core oblateness of the Moon (f_c) differ by about 12% with respect to the INPOP17a solution for the same fixed core polar moment ratio as in INPOP17a ($\frac{C_c}{C_T} = 7\times10^{-4}$) and remains consistent with a recent in-house analysis [21] involving an improved lunar interior paramaterization and a more complex torque modeling.

LLR data are not explicity used for ITRF solutions. However, some stations contribute other data products (GPS,SLR,VLBI) to the ITRF solutions. Stations with a long temporal baseline in LLR allow the fit of their coordinates (and in some cases, velocities) to the LLR data. Table 8 gives the list of station and reflector coordinates used for the INPOP19a solution. The INPOP17a document [19] contains a typographic error on reference values of the Lunokhod 1 and 2 reflector coordinates[3]. Users of the older INPOP17a solution must use their respective PA coordinates (XYZ in m) as $L1_{XYZ}$=1114292.5047, -781298.2434, 1076058.5100 and $L2_{XYZ}$=1339363.4749, 801872.1138, 756358.5308.

References

[1] Steven R. Chesley, James Baer, and David G. Monet. Treatment of star catalog biases in asteroid astrometric observations. Icarus, 210(1):158–181, Nov 2010.

[2] Daniele Durante, D. J. Hemingway, P. Racioppa, L. Iess, and D. J. Stevenson. Titan's gravity field and interior structure after Cassini. Icarus, 326:123–132, Jul 2019.

[3] A. Fienga, C. Avdellidou, and J. Hanus. Asteroid masses obtained with inpop planetary ephemerides. ArXiv e-prints:1601.00947, 2019.

[4] A. Fienga, J. Laskar, H. Manche, M. Gastineau, and A. Verma. DPAC INPOP final release: INPOP10e. ArXiv e-prints , 2012.

[5] A. Fienga, J. Laskar, H. Manche, P. Kuchynka, G. Desvignes, M. Gastineau, I. Cognard, and G. Thereau. The planetary ephemerides INPOP10a and its applications in fundamental physics. Celest. Mech. Dyn. Astron., 111:363–+, 2011.

[3] personal communication, D.Pavlov, IAA RAS

Table 1: INPOP19a data samples used for its adjustments. The columns 1 and 2 give the observed planet and an information on the space mission providing the observations. Columns 3 and 4 give the number of observations and the time interval, while the column 5gives the *a priori* uncertainties provided by space agencies or the navigation teams. Finally in the last two columns, are given the WRMS for INPOP19a and INPOP17a.

Planet / Type	#	Period	Averaged	WRMS	
			Accuracy	INPOP19a	INPOP17a
Mercury					
Direct range [m]	462	1971.29 : 1997.60	900	0.95	0.96
Messenger range [m]	1096	2011.23 : 2014.26	5	0.82	1.29
Mariner range [m]	2	1974.24 : 1976.21	100	0.37	0.78
Venus					
VLBI [mas]	68	1990.70 : 2013.14	2.0	1.13	1.178
Direct range [m]	489	1965.96 : 1990.07	1400	0.98	0.98
Vex range [m]	24783	2006.32 : 2011.45	7.0	0.93	0.93
Mars					
VLBI [mas]	194	1989.13 : 2013.86	0.3	1.26	1.16
Mex range [m]	30669	2005.17 : 2017.37	2.0	0.98	3.37
		2005.17 : 2016.37	2.0	0.97	1.26
MGS range [m]	2459	1999.31 : 2006.70	2.0	0.93	1.31
MRO/MO range [m]	20985	2002.14 : 2014.00	1.2	1.07	1.91
Jupiter					
VLBI [mas]	24	1996.54 : 1997.94	11	1.01	1.03
Optical ra/de [arcsec]	6416	1924.34 : 2008.49	0.3	1.0	1.0
Flybys ra/de [mas]	5	1974.92 : 2001.00	4.0/12.0	0.94/1.0	0.58/0.82
Flybys range [m]	5	1974.92 : 2001.00	2000	0.98	0.71
Juno range [m]	9	2016.65 : 2018.68	20	0.945	116.0
Saturn					
Optical ra/de [arcsec]	7826	1924.22 : 2008.34	0.3	0.96/0.87	0.96/0.87
Cassini					
VLBI ra/de [mas]	10	2004.69 : 2009.31	0.6/0.3	0.97/0.99	0.92/0.91
JPL range [m]	165	2004.41 : 2014.38	25.0	0.99	1.01
Grand Finale range [m]	9	2017.35 : 2017.55	3.0	1.14	29.0
La Sapienza range [m]	614	2006.01 : 2016.61	6.0	1.01	2.64
Uranus					
Optical ra/de [arcsec]	12893	1924.62 : 2011.74	0.2/0.3	1.09 / 0.82	1.09 / 0.82
Flybys ra/de [mas]	1	1986.07 : 1986.07	50/50	0.12 / 0.42	0.42 /1.23
Flybys range [m]	1	1986.07 : 1986.07	50	0.92	0.002
Neptune					
Optical ra/de [arcsec]	5254	1924.04 : 2007.88	0.25/0.3	1.008 / 0.97	1.008 / 0.97
Flybys ra/de [mas]	1	1989.65 : 1989.65	15.0	0.11 / 0.15	1.0/1.57
Flybys range [m]	1	1989.65 : 1989.65	2	1.14	1.42

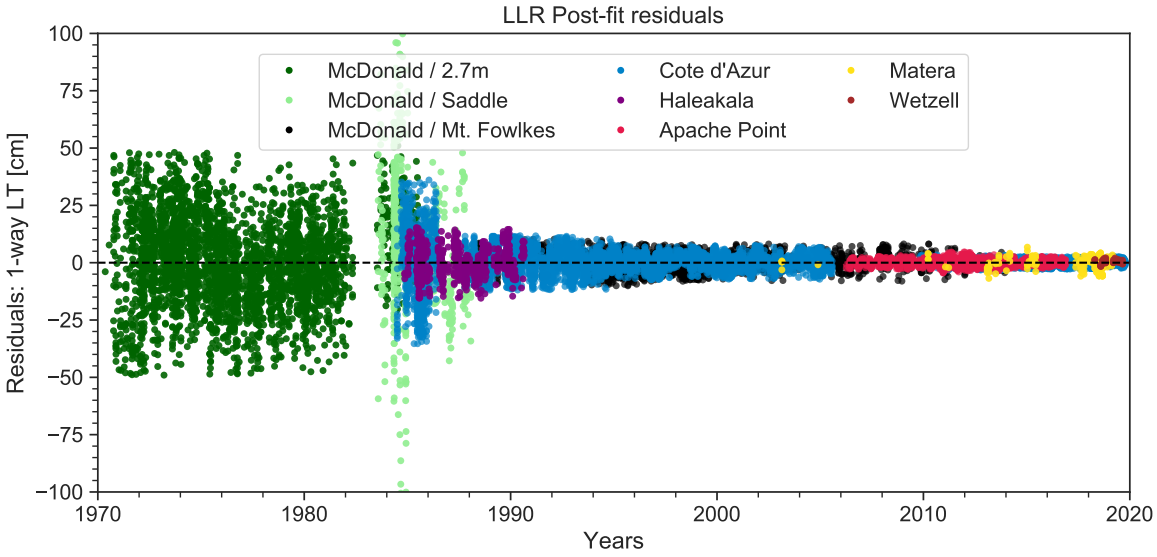

Figure 5: LLR post-fit residuals obtained with INPOP19a (wrms in cm) from 1969 to 2019.

TNO	GM AU^3d^{-2}	mass kg
50000	7.235460e-14	4.863611e+20
55637	1.880380e-14	1.263975e+20
90482	9.554830e-14	6.422671e+20
120347	1.934696e-14	1.300485e+20
136108	6.036990e-13	4.058011e+21
136199	2.519160e-12	1.693357e+22
174567	3.994670e-14	2.685181e+20
208996	8.007340e-14	5.382462e+20
136472	4.498510e-13	3.023858e+21

Table 2: Masses for the nine biggest TNO kept fixed in INPOP19a. Values extracted from [17].

Table 3: Values of parameters obtained in the fit of INPOP13c, INPOP10e, DE430 and DE436 to observations.

	INPOP13c $\pm 1\sigma$	INPOP17a $\pm 1\sigma$	INPOP19a $\pm 1\sigma$	DE436 $\pm 1\sigma$
(EMRAT-81.3000)$\times 10^{-4}$	(5.694 ± 0.010)	(5.719 ± 0.010)	(5.668 ± 0.010)	5.68217
$J_2^{\odot} \times 10^{-7}$	(2.30 ± 0.25)	(2.295 ± 0.010)	(2.010 ± 0.010)	NC
$GM_{\odot}$ - 132712440000 [$km^3.\ s^{-2}$]	(44.487 ± 0.17)	(42.693 ± 0.04)	(40.042 ± 0.01)	41.939377

Table 4: Euler angles fitted by comparing two planet ephemerides different only by the asteroid orbits used for computing their perturbations on the planet orbits: one being fitted over the Gaia DR2 and one obtained from the astorb data base.

	θ	ψ	ϕ
	μas	μas	μas
All planets	-98 ± 1508	1.0 ± 45	253 ± 3971
Inner planets	1.16 ± 0.20	-0.08 ± 0.62	-1.50 ± 0.150
Inner planets + Jupiter	1.23 ± 0.16	-1.0 ± 0.22	-0.128 ± 0.69
Inner planets + Jupiter + Saturn	1.83 ± 0.80	1.057 ± 0.053	-0.23 ± 2.56
Outer planets	-55 ± 629	-30 ± 495	373 ± 5051

Table 5: Comparison of LLR post-fit residuals (wrms in cm) of LLR observations between INPOP17a (1969-2017) and INPOP19a (1969-2019). INPOP17a statistics are drawn from [20].

Station	Time span	INPOP17a		INPOP19a	
		Used	wrms	Used	wrms
APOLLO	2006-2010	929	1.27	925	1.19
APOLLO	2010-2012	486	1.95	496	1.76
APOLLO	2012-2013	345	1.52	347	1.42
APOLLO	2013-2016	800	1.15	816	1.02
Grasse	1984-1986	1161	14.01	1098	14.18
Grasse	1987-1995	3407	4.11	3386	4.62
Grasse	1995-2006	4754	2.86	4831	2.84
Grasse	2009-2013	982	1.41	981	1.30
Grasse	2013-2017	3320	1.51	3420	1.06
Grasse	2017-2019	-	-	3302	1.02
Haleakala	1984-1990	728	4.80	737	6.08
Matera	2003-2013	37	2.37	37	2.21
Matera	2013-2015	30	2.93	27	2.39
Matera	2015-2019	-	-	154	2.40
McDonald	1969-1983	3246	18.87	3276	18.57
McDonald	1983-1986	148	16.77	155	14.31
MLRS1	1983-1984	44	32.73	44	31.00
MLRS2	1984-1985	356	62.58	347	54.80
MLRS2	1985-1989	202	11.07	219	18.23
MLRS2	1988-1997	1162	3.81	1182	3.86
MLRS2	1997-2013	1939	3.72	1933	3.10
MLRS2	2013-2016	15	2.59	15	2.35
Wettzell	2018-2019	-	-	52	0.88

Table 6: Parameters for the Earth-Moon system.

Parameter	Units	INPOP17a	INPOP19a
GM_{EMB}	au^3/d^2	8.997011404E-10	8.997011394E-10
$\tau_{R1,E}$	d	7.36E-03	7.98E-03
$\tau_{R2,E}$	d	2.89E-03	2.82E-03
$C_T/(MR^2)$		3.93148E-01	3.93140E-01
C_{32}		4.84441E-06	4.84500E-06
S_{32}		1.683E-06	1.685E-06
C_{33}		1.6877E-06	1.6686E-06
τ_M	d	8.7E-02	9.4E-02
k_v/C_T	d^{-1}	1.75E-08	1.64E-08
f_c		2.5E-04	2.8E-04
h_2		4.38E-02	4.26E-02

Table 7: Amplitudes of periodic terms as corrections to longitude librations (in mas) obtained between ephemeris solutions to account for frequency-dependent dissipation in the Moon, where the polynomial expansion of the Delaunay arguments l' (solar mean anomaly), l (lunar mean anomaly), F (argument of latitude) and D (mean elongation of the Moon from the Sun) follow Eqn. 5.43 in [16]. Columns labeled as DE430, WB2015, EPM2015 and EPM2017 were obtained from [7], [24], [15] and the IAA RAS website, respectively.

Parameter	Period	Longitude libration correction (in mas)				
	(d)	DE430	WB2015	EPM2015	EPM2017	INPOP19a
$A_1\cos(l')$	365.26	5.0 ± 1.3	4.9 ± 1.1	4.5 ± 0.2	4.4	4.4 ± 0.6
$A_2\cos(2l-2D)$	205.89	1.5 ± 1.2	2.0 ± 1.2	1.4 ± 0.2	1.6	1.7 ± 0.9
$A_3\cos(2F-2l)$	1095.22	-3.6 ± 3.3	0.7 ± 6.2	-7.3 ± 0.5	-5.2	9.7 ± 4.4

Table 8: Station and lunar surface reflector coordinates used for the fits of INPOP19a solution.

Earth Station	x	y	z	$\dot{x}$	$\dot{y}$	$\dot{z}$
APOLLO	-1463998.9085	-5166632.7635	3435012.8835	-0.0141	0.0003	-0.0022
Grasse	4581692.1675	556196.0730	4389355.1088	-0.0151	0.0191	0.0118
Haleakala	-5466003.7191	-2404425.9369	2242197.9030	-0.0122	0.0622	0.0310
Matera	4641978.8100	1393067.5310	4133249.4800	-0.0180	0.0192	0.0140
McDonald	-1330781.5567	-5328756.3783	3235697.9118	-0.0227	0.0277	0.0139
MLRS1	-1330120.9826	-5328532.3644	3236146.0080	-0.0124	0.0009	-0.0053
MLRS2	-1330021.4931	-5328403.3401	3236481.6472	-0.0129	0.0015	-0.0036
Wettzell	4075576.7587	931785.5077	4801583.6067	-0.0139	0.0170	0.0124
Lunar reflector	**x**	**y**	**z**			
Apollo 11	1591966.6111	690699.5452	21003.7497			
Lunokhod 1	1114292.2641	-781298.3844	1076058.6360			
Apollo 14	1652689.5835	-520997.5017	-109730.5271			
Apollo 15	1554678.3047	98095.6097	765005.2064			
Lunokhod 2	1339363.3642	801872.0049	756358.6487			

Table 9: Estimated values of station biases over different periods (2-way light time in cm).

Bias #	Station	Date	Bias 2-way light time [cm]	
			INPOP17a	INPOP19a
1	APOLLO	2006/04/07 - 2010/11/01	-0.24	0.27
2		2007/12/15 - 2008/06/30	-3.90	-3.95
3		2008/09/20 - 2009/06/20	2.83	3.22
4		2010/11/01 - 2012/04/07	-5.98	-6.03
5		2012/04/07 - 2013/09/02	9.12	8.99
6	Grasse	1984/06/01 - 1986/06/13	-6.49	16.99
7		1987/10/01 - 2005/08/01	2.47	-5.00
8		1993/03/01 - 1996/10/01	10.38	9.36
9		1996/12/10 - 1997/01/18	16.92	14.04
10		1997/02/08 - 1998/06/24	19.56	20.39
11		2004/12/04 - 2004/12/07	-7.07	-5.28
12		2005/01/03 - 2005/01/06	-6.72	-4.38
13		2009/11/01 - 2014/01/01	0.34	-0.94
14		2015/12/20 - 2015/12/21	-88.34	-88.05
15	Haleakala	1984/11/01 - 1990/09/01	2.55	9.54
16		1984/11/01 - 1986/04/01	-3.61	-1.84
17		1986/04/02 - 1987/07/30	13.07	9.52
18		1987/07/31 - 1987/08/14	1.83	2.57
19		1985/06/09 - 1985/06/10	-13.18	-11.03
20		1987/11/10 - 1988/02/18	19.49	17.32
21		1990/02/06 - 1990/09/01	14.32	11.68
22	Matera	2003/01/01 - 2016/01/01	4.62	0.06
23	McDonald	1969/01/01 - 1985/07/01	-37.88	-45.21
24		1971/12/01 - 1972/12/05	28.21	38.03
25		1972/04/21 - 1972/04/27	88.09	130.6
26		1974/08/18 - 1974/10/16	-112.08	-116.54
27		1975/10/05 - 1976/03/01	28.44	26.68
28		1983/12/01 - 1984/01/17	11.06	-3.94
29		1969/01/01 - 1971/12/31	2249.19	2266.53
30	MLRS1	1983/08/01 - 1988/01/28	38.73	12.89

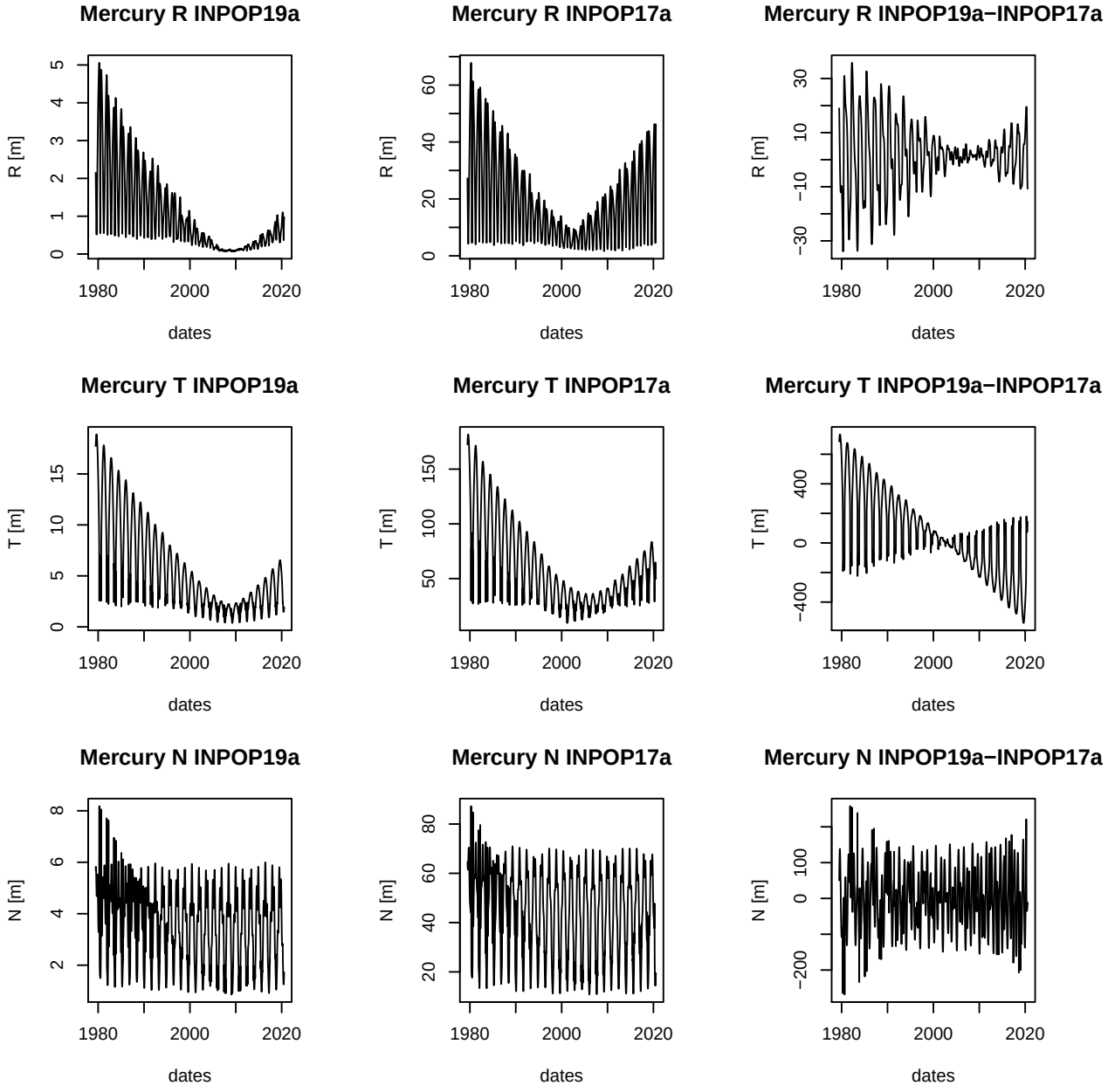

Figure 6: Propagation of least squares standard dispersion for the orbit of Mercury in the case of INPOP19a and INPOP17a. Right-hand side plots give the geocentric differences for Mercury (INPOP19a-INPOP17a) integrated positions. All the differences and Propagation of least squares standard dispersion are given in (R,T,N) geocentric frame.

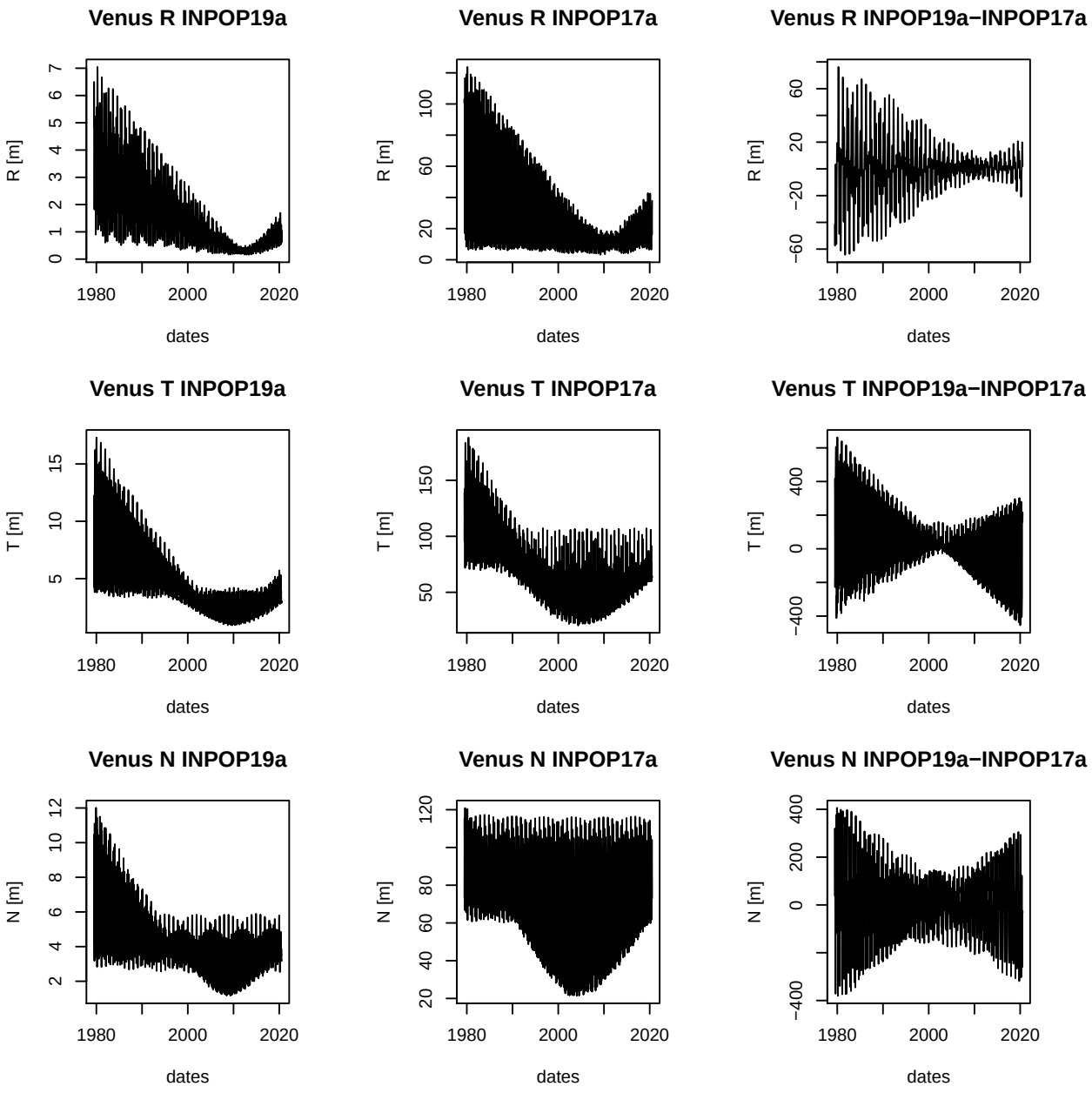

Figure 7: Propagation of least squares standard dispersion for the orbit of Venus in the case of INPOP19a and INPOP17a. Right-hand side plots give the geocentric differences for Venus (INPOP19a-INPOP17a) integrated positions. All the differences and propagation of least squares standard dispersion are given in (R,T,N) geocentric frame.

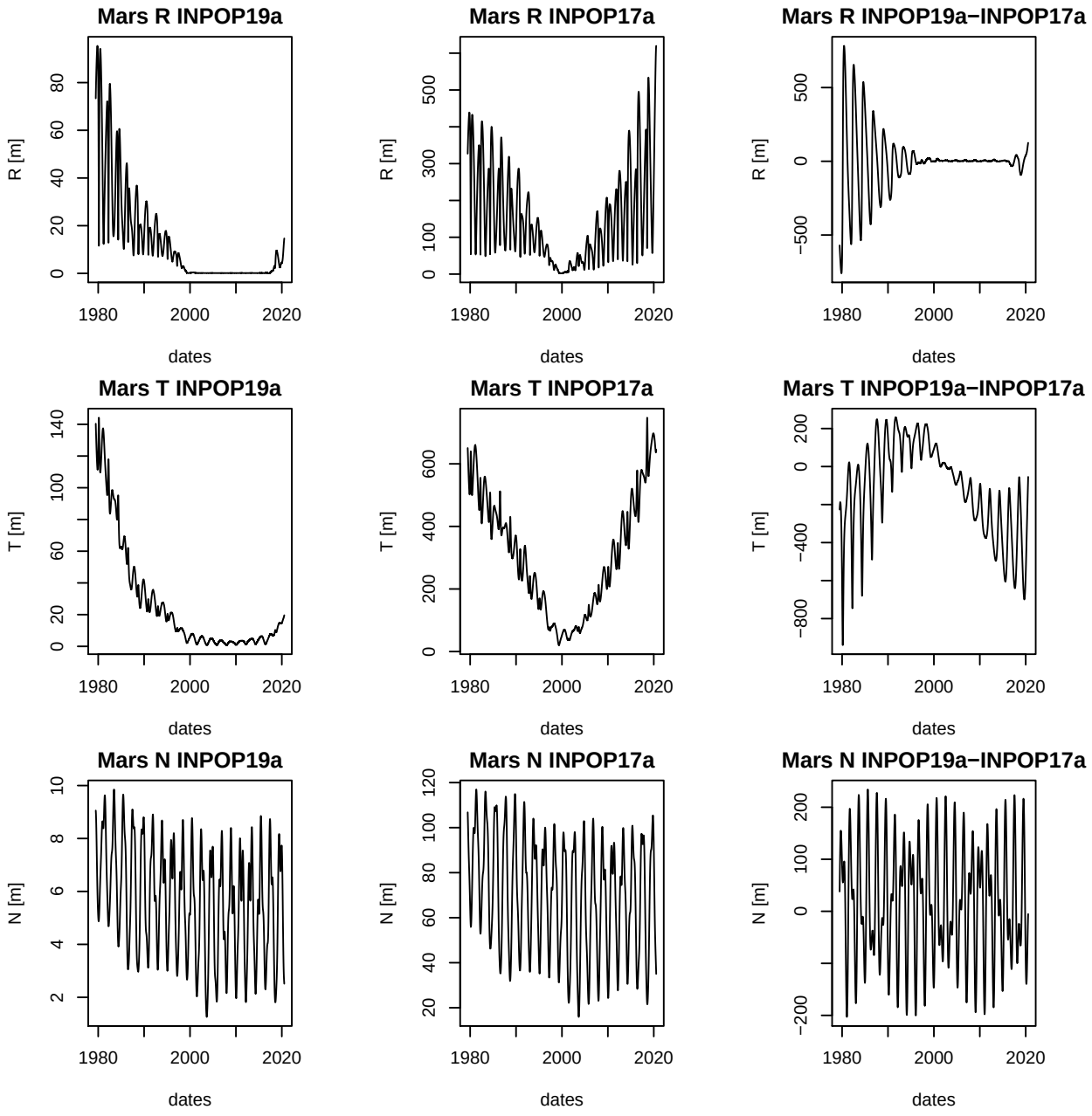

Figure 8: Propagation of least squares standard dispersion for the orbit of Mars in the case of INPOP19a and INPOP17a. Right-hand side plots give the geocentric differences for Mars (INPOP19a-INPOP17a) integrated positions. All the differences and propagation of least squares standard dispersion are given in (R,T,N) geocentric frame for Mars and (R,T,N) barycentric frame for EMB.

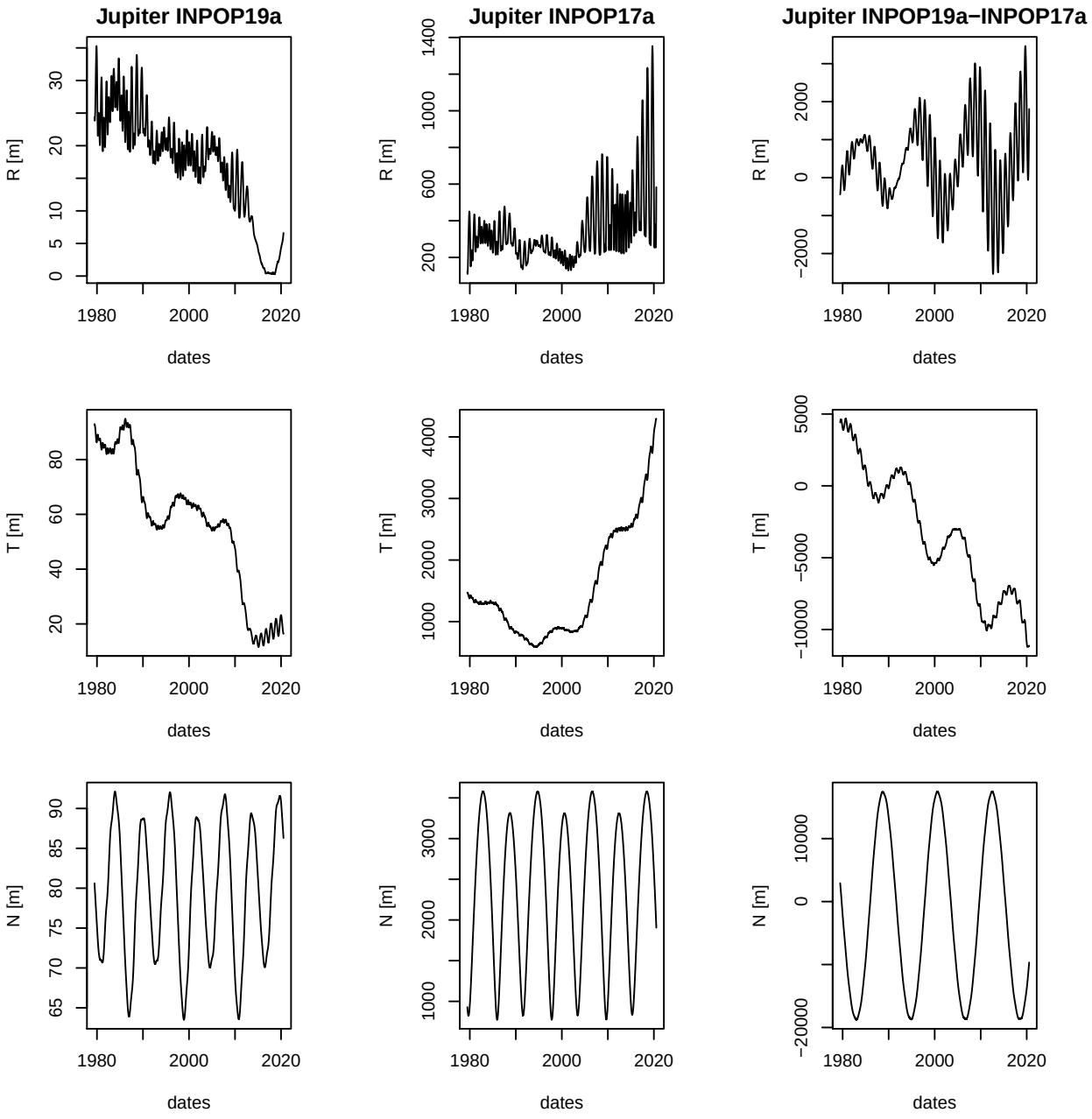

Figure 9: Propagation of least squares standard dispersion for the orbit of Jupiter in the case of INPOP19a and INPOP17a. Right-hand side plots give the geocentric differences for Jupiter (INPOP19a-INPOP17a) integrated positions. All the differences and propagation of least squares standard dispersion are given in (R,T,N) geocentric frame.

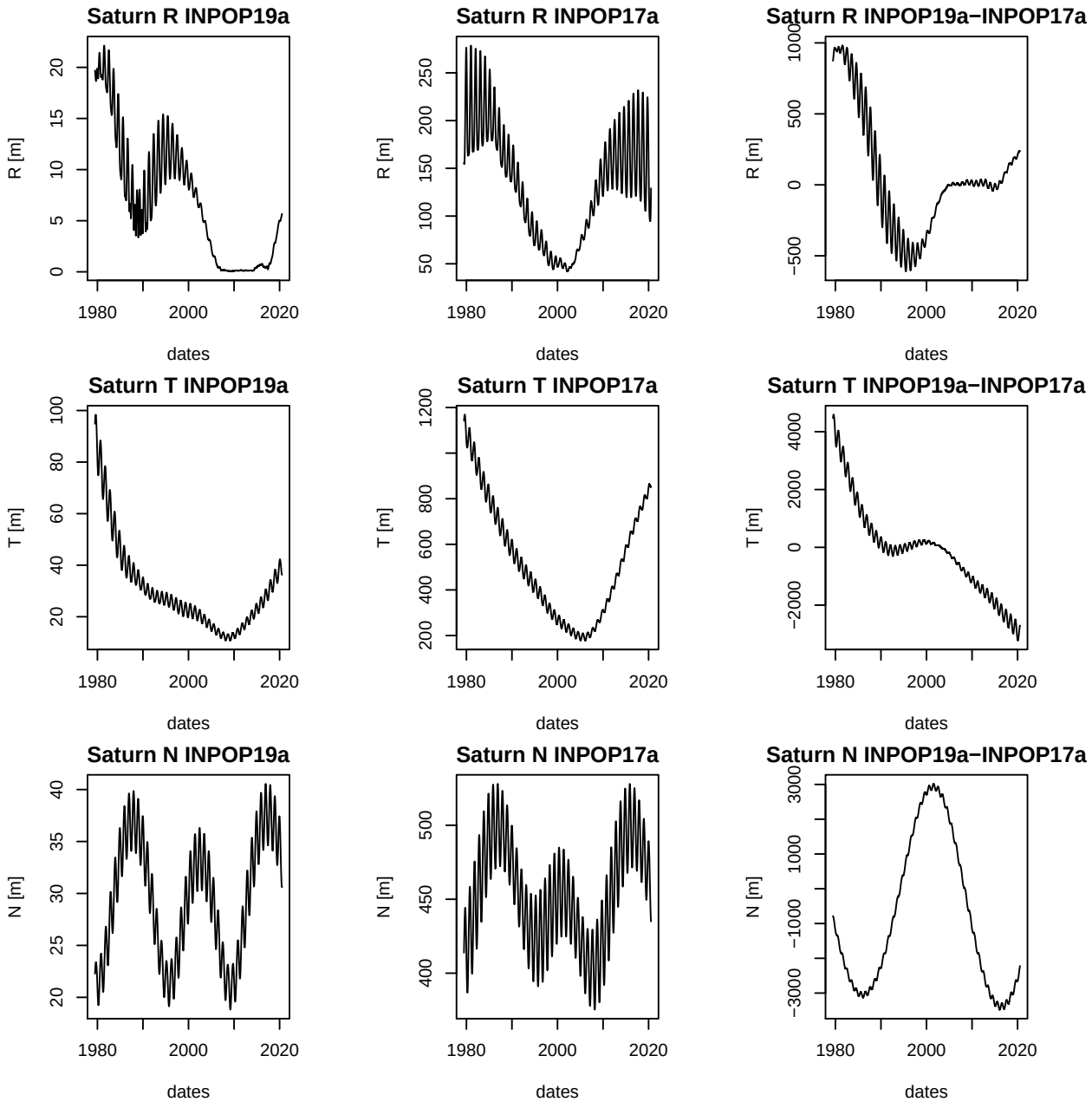

Figure 10: Propagation of least squares standard dispersion for the orbit of Saturn in the case of INPOP19a and INPOP17a. Right-hand side plots give the geocentric differences for Saturn (INPOP19a-INPOP17a) integrated positions. All the differences and propagation of least squares standard dispersion are given in (R,T,N) geocentric frame.

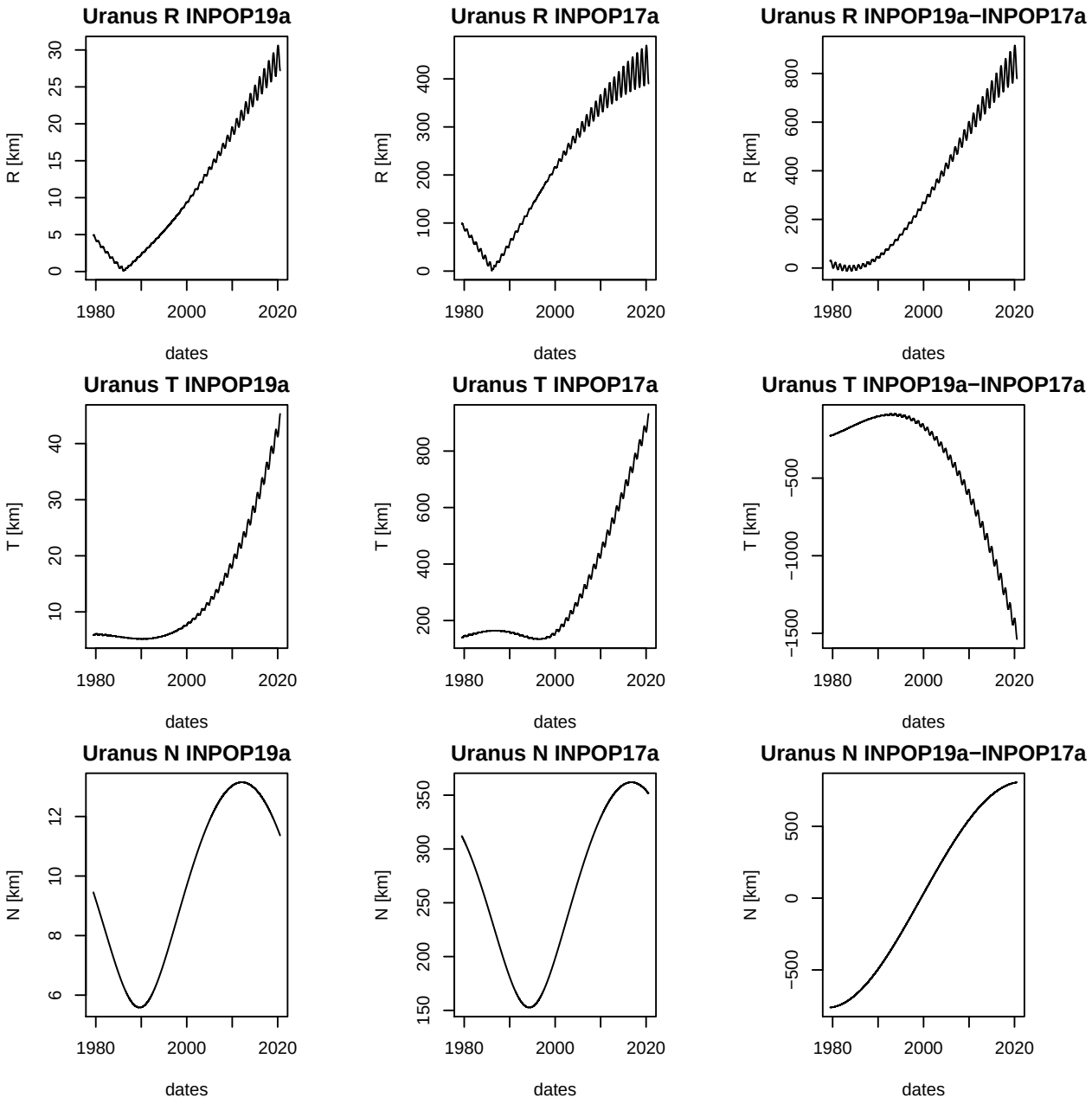

Figure 11: Propagation of least squares standard dispersion for the orbit of Uranus in the case of INPOP19a and INPOP17a. Right-hand side plots give the geocentric differences for Uranus (INPOP19a-INPOP17a) integrated positions. All the differences and propagation of least squares standard dispersion are given in (R,T,N) geocentric frame.

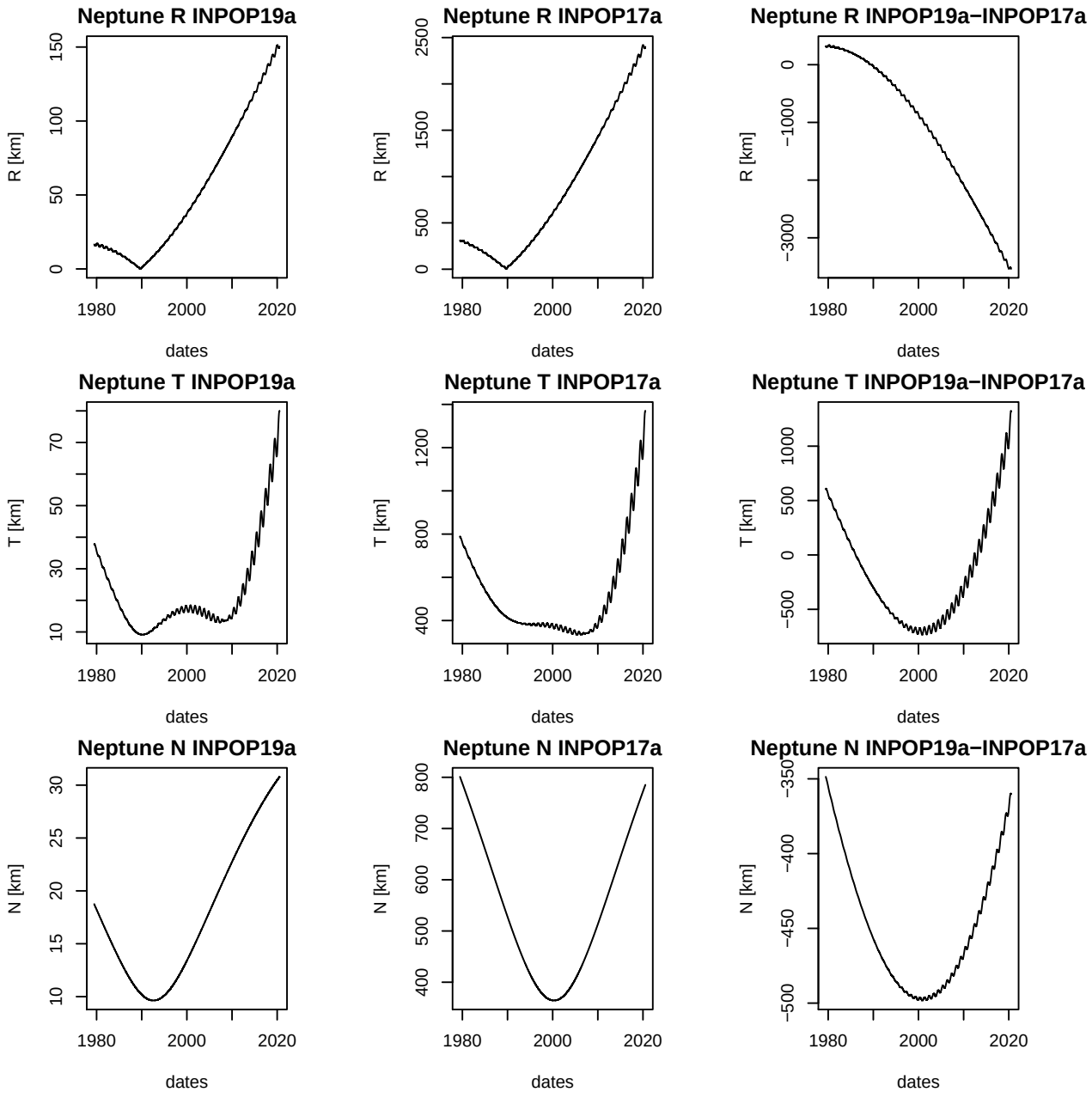

Figure 12: Propagation of least squares standard dispersion for the orbit of Neptune in the case of INPOP19a and INPOP17a. Right-hand side plots give the geocentric differences for Neptune (INPOP19a-INPOP17a) integrated positions. All the differences and propagation of least squares standard dispersion are given in (R,T,N) geocentric frame.

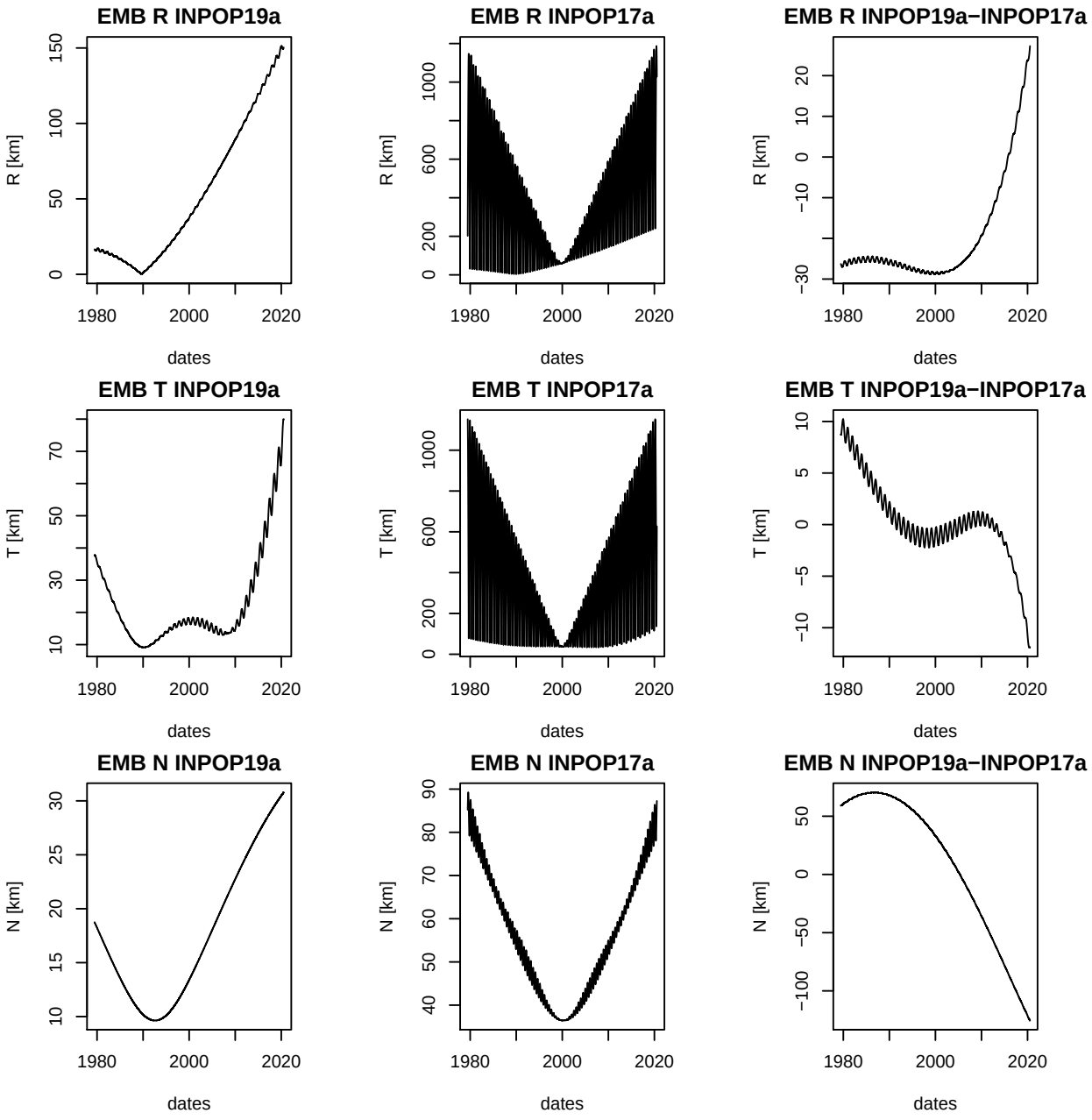

Figure 13: Propagation of least squares standard dispersion for the orbit of EMB versus SSB in the case of INPOP19a and INPOP17a. Right-hand side plots give the SSB differences for EMB (INPOP19a-INPOP17a) integrated positions. All the differences and propagation of least squares standard dispersion are given in (R,T,N) barycentric frame.

[6] W. M. Folkner, L. Iess, J. D. Anderson, S. W. Asmar, D. R. Buccino, D. Durante, M. Feldman, L. Gomez Casajus, M. Gregnanin, A. Milani, M. Parisi, R. S. Park, D. Serra, G. Tommei, P. Tortora, M. Zannoni, S. J. Bolton, J. E. P. Connerney, and S. M. Levin. Jupiter gravity field estimated from the first two juno orbits. Geophysical Research Letters, 44(10):4694–4700, 2017.

[7] W. M. Folkner, J. G. Williams, D. H. Boggs, R. S. Park, and P. Kuchynka. The Planetary and Lunar Ephemerides DE430 and DE431. Interplanetary Network Progress Report, 196:C1, February 2014.

[8] Gaia Collaboration, Mignard, F., Klioner, S. A., Lindegren, L., Hernández, J., Bastian, U., Bombrun, A., Hobbs, D., Lammers, U., Michalik, D., Ramos-Lerate, M., Biermann, M., Fernández-Hernández, J., Geyer, R., Hilger, T., Siddiqui, H. I., Steidelmüller, H., Babusiaux, C., Barache, C., Lambert, S., Andrei, A. H., Bourda, G., Charlot, P., Brown, A. G. A., Vallenari, A., Prusti, T., de Bruijne, J. H. J., Bailer-Jones, C. A. L., Evans, D. W., Eyer, L., Jansen, F., Jordi, C., Luri, X., Panem, C., Pourbaix, D., Randich, S., Sartoretti, P., Soubiran, C., van Leeuwen, F., Walton, N. A., Arenou, F., Cropper, M., Drimmel, R., Katz, D., Lattanzi, M. G., Bakker, J., Cacciari, C., Castañeda, J., Chaoul, L., Cheek, N., De Angeli, F., Fabricius, C., Guerra, R., Holl, B., Masana, E., Messineo, R., Mowlavi, N., Nienartowicz, K., Panuzzo, P., Portell, J., Riello, M., Seabroke, G. M., Tanga, P., Thévenin, F., Gracia-Abril, G., Comoretto, G., Garcia-Reinaldos, M., Teyssier, D., Altmann, M., Andrae, R., Audard, M., Bellas-Velidis, I., Benson, K., Berthier, J., Blomme, R., Burgess, P., Busso, G., Carry, B., Cellino, A., Clementini, G., Clotet, M., Creevey, O., Davidson, M., De Ridder, J., Delchambre, L., Dell´Oro, A., Ducourant, C., Fouesneau, M., Frémat, Y., Galluccio, L., García-Torres, M., González-Núñez, J., González-Vidal, J. J., Gosset, E., Guy, L. P., Halbwachs, J.-L., Hambly, N. C., Harrison, D. L., Hestroffer, D., Hodgkin, S. T., Hutton, A., Jasniewicz, G., Jean-Antoine-Piccolo, A., Jordan, S., Korn, A. J., Krone-Martins, A., Lanzafame, A. C., Lebzelter, T., Löffler, W., Manteiga, M., Marrese, P. M., Martín-Fleitas, J. M., Moitinho, A., Mora, A., Muinonen, K., Osinde, J., Pancino, E., Pauwels, T., Petit, J.-M., Recio-Blanco, A., Richards, P. J., Rimoldini, L., Robin, A. C., Sarro, L. M., Siopis, C., Smith, M., Sozzetti, A., Süveges, M., Torra, J., van Reeven, W., Abbas, U., Abreu Aramburu, A., Accart, S., Aerts, C., Altavilla, G., Álvarez, M. A., Alvarez, R., Alves, J., Anderson, R. I., Anglada Varela, E., Antiche, E., Antoja, T., Arcay, B., Astraatmadja, T. L., Bach, N., Baker, S. G., Balaguer-Núñez, L., Balm, P., Barata, C., Barbato, D., Barblan, F., Barklem, P. S., Barrado, D., Barros, M., Barstow, M. A., Bartholomé Muñoz, L., Bassilana, J.-L., Becciani, U., Bellazzini, M., Berihuete, A., Bertone, S., Bianchi, L., Bienaymé, O., Blanco-Cuaresma, S., Boch, T., Boeche, C., Borrachero, R., Bossini, D., Bouquillon, S., Bragaglia, A., Bramante, L., Breddels, M. A., Bressan, A., Brouillet, N., Brüsemeister, T., Brugaletta, E., Bucciarelli, B., Burlacu, A., Busonero, D., Butkevich, A. G., Buzzi, R., Caffau, E., Cancelliere, R., Cannizzaro, G., Cantat-Gaudin, T., Carballo, R., Carlucci, T., Carrasco, J. M., Casamiquela, L., Castellani, M., Castro-Ginard, A., Chemin, L., Chiavassa, A., Cocozza, G., Costigan, G., Cowell, S., Crifo, F., Crosta, M., Crowley, C., Cuypers, J., Dafonte, C., Damerdji, Y., Dapergolas, A., David, P., David, M., de Laverny, P., De Luise, F., De March, R., de Souza, R., de Torres, A., Debosscher, J., del Pozo, E., Delbo, M., Delgado, A., Delgado, H. E., Diakite, S., Diener, C., Distefano, E., Dolding, C., Drazinos, P., Durán, J., Edvardsson, B., Enke, H., Eriksson, K., Esquej, P., Eynard Bontemps, G., Fabre, C., Fabrizio, M., Faigler, S., Falcão, A. J., Farràs Casas, M., Federici, L., Fedorets, G., Fernique, P., Figueras, F., Filippi, F., Findeisen, K., Fonti, A., Fraile, E., Fraser, M., Frézouls, B., Gai, M., Galleti, S., Garabato, D., García-Sedano, F., Garofalo, A., Garralda, N., Gavel, A., Gavras, P., Gerssen, J., Giacobbe, P., Gilmore, G., Girona, S., Giuffrida, G., Glass, F., Gomes, M., Granvik, M., Gueguen, A., Guerrier, A., Guiraud, J., Gutié, R., Haigron, R., Hatzidimitriou, D., Hauser, M., Haywood, M., Heiter,

U., Helmi, A., Heu, J., Hofmann, W., Holland, G., Huckle, H. E., Hypki, A., Icardi, V., Janßen, K., Jevardat de Fombelle, G., Jonker, P. G., Juhász, A. L., Julbe, F., Karampelas, A., Kewley, A., Klar, J., Kochoska, A., Kohley, R., Kolenberg, K., Kontizas, M., Kontizas, E., Koposov, S. E., Kordopatis, G., Kostrzewa-Rutkowska, Z., Koubsky, P., Lanza, A. F., Lasne, Y., Lavigne, J.-B., Le Fustec, Y., Le Poncin-Lafitte, C., Lebreton, Y., Leccia, S., Leclerc, N., Lecoeur-Taibi, I., Lenhardt, H., Leroux, F., Liao, S., Licata, E., Lindstrøm, H. E. P., Lister, T. A., Livanou, E., Lobel, A., López, M., Managau, S., Mann, R. G., Mantelet, G., Marchal, O., Marchant, J. M., Marconi, M., Marinoni, S., Marschalkó, G., Marshall, D. J., Martino, M., Marton, G., Mary, N., Massari, D., Matijevic, G., Mazeh, T., McMillan, P. J., Messina, S., Millar, N. R., Molina, D., Molinaro, R., Molnár, L., Montegriffo, P., Mor, R., Morbidelli, R., Morel, T., Morris, D., Mulone, A. F., Muraveva, T., Musella, I., Nelemans, G., Nicastro, L., Noval, L., O´Mullane, W., Ordénovic, C., Ordóñez-Blanco, D., Osborne, P., Pagani, C., Pagano, I., Pailler, F., Palacin, H., Palaversa, L., Panahi, A., Pawlak, M., Piersimoni, A. M., Pineau, F.-X., Plachy, E., Plum, G., Poggio, E., Poujoulet, E., Prsa, A., Pulone, L., Racero, E., Ragaini, S., Rambaux, N., Regibo, S., Reylé, C., Riclet, F., Ripepi, V., Riva, A., Rivard, A., Rixon, G., Roegiers, T., Roelens, M., Romero-Gómez, M., Rowell, N., Royer, F., Ruiz-Dern, L., Sadowski, G., Sagristà Sellés, T., Sahlmann, J., Salgado, J., Salguero, E., Sanna, N., Santana-Ros, T., Sarasso, M., Savietto, H., Schultheis, M., Sciacca, E., Segol, M., Segovia, J. C., Ségransan, D., Shih, I.-C., Siltala, L., Silva, A. F., Smart, R. L., Smith, K. W., Solano, E., Solitro, F., Sordo, R., Soria Nieto, S., Souchay, J., Spagna, A., Spoto, F., Stampa, U., Steele, I. A., Stephenson, C. A., Stoev, H., Suess, F. F., Surdej, J., Szabados, L., Szegedi-Elek, E., Tapiador, D., Taris, F., Tauran, G., Taylor, M. B., Teixeira, R., Terrett, D., Teyssandier, P., Thuillot, W., Titarenko, A., Torra Clotet, F., Turon, C., Ulla, A., Utrilla, E., Uzzi, S., Vaillant, M., Valentini, G., Valette, V., van Elteren, A., Van Hemelryck, E., van Leeuwen, M., Vaschetto, M., Vecchiato, A., Veljanoski, J., Viala, Y., Vicente, D., Vogt, S., von Essen, C., Voss, H., Votruba, V., Voutsinas, S., Walmsley, G., Weiler, M., Wertz, O., Wevers, T., Wyrzykowski, L., Yoldas, A., Zerjal, M., Ziaeepour, H., Zorec, J., Zschocke, S., Zucker, S., Zurbach, C., and Zwitter, T. Gaia data release 2 - the celestial reference frame (gaia-crf2). A&A, 616:A14, 2018.

[9] Gaia Collaboration, F. Spoto, P. Tanga, F. Mignard, J. Berthier, B. Carry, A. Cellino, A. Dell'Oro, D. Hestroffer, K. Muinonen, T. Pauwels, J. M. Petit, P. David, F. De Angeli, M. Delbo, B. Frézouls, L. Galluccio, M. Granvik, J. Guiraud, J. Hernández, C. Ordénovic, J. Portell, E. Poujoulet, W. Thuillot, G. Walmsley, A. G. A. Brown, A. Vallenari, T. Prusti, J. H. J. de Bruijne, C. Babusiaux, C. A. L. Bailer-Jones, M. Biermann, D. W. Evans, L. Eyer, F. Jansen, C. Jordi, S. A. Klioner, U. Lammers, L. Lindegren, X. Luri, C. Panem, D. Pourbaix, S. Randich, P. Sartoretti, H. I. Siddiqui, C. Soubiran, F. van Leeuwen, N. A. Walton, F. Arenou, U. Bastian, M. Cropper, R. Drimmel, D. Katz, M. G. Lattanzi, J. Bakker, C. Cacciari, J. Castañeda, L. Chaoul, N. Cheek, C. Fabricius, R. Guerra, B. Holl, E. Masana, R. Messineo, N. Mowlavi, K. Nienartowicz, P. Panuzzo, M. Riello, G. M. Seabroke, F. Thévenin, G. Gracia-Abril, G. Comoretto, M. Garcia-Reinaldos, D. Teyssier, M. Altmann, R. Andrae, M. Audard, I. Bellas-Velidis, K. Benson, R. Blomme, P. Burgess, G. Busso, G. Clementini, M. Clotet, O. Creevey, M. Davidson, J. De Ridder, L. Delchambre, C. Ducourant, J. Fernández-Hernández, M. Fouesneau, Y. Frémat, M. García-Torres, J. González-Núñez, J. J. González-Vidal, E. Gosset, L. P. Guy, J. L. Halbwachs, N. C. Hambly, D. L. Harrison, S. T. Hodgkin, A. Hutton, G. Jasniewicz, A. Jean-Antoine-Piccolo, S. Jordan, A. J. Korn, A. Krone-Martins, A. C. Lanzafame, T. Lebzelter, W. Lö, M. Manteiga, P. M. Marrese, J. M. Martín-Fleitas, A. Moitinho, A. Mora, J. Osinde, E. Pancino, A. Recio-Blanco, P. J. Richards, L. Rimoldini, A. C. Robin, L. M. Sarro, C. Siopis, M. Smith, A. Sozzetti, M. Süveges, J. Torra, W. van Reeven, U. Abbas, A. Abreu Aramburu, S. Accart, C. Aerts, G. Altavilla, M. A. Álvarez, R. Alvarez, J. Alves, R. I. Anderson,

A. H. Andrei, E. Anglada Varela, E. Antiche, T. Antoja, B. Arcay, T. L. Astraatmadja, N. Bach, S. G. Baker, L. Balaguer-Núñez, P. Balm, C. Barache, C. Barata, D. Barbato, F. Barblan, P. S. Barklem, D. Barrado, M. Barros, M. A. Barstow, L. Bartholomé Muñoz, J. L. Bassilana, U. Becciani, M. Bellazzini, A. Berihuete, S. Bertone, L. Bianchi, O. Bienaymé, S. Blanco-Cuaresma, T. Boch, C. Boeche, A. Bombrun, R. Borrachero, D. Bossini, S. Bouquillon, G. Bourda, A. Bragaglia, L. Bramante, M. A. Breddels, A. Bressan, N. Brouillet, T. Brüsemeister, E. Brugaletta, B. Bucciarelli, A. Burlacu, D. Busonero, A. G. Butkevich, R. Buzzi, E. Caffau, R. Cancelliere, G. Cannizzaro, T. Cantat-Gaudin, R. Carballo, T. Carlucci, J. M. Carrasco, L. Casamiquela, M. Castellani, A. Castro-Ginard, P. Charlot, L. Chemin, A. Chiavassa, G. Cocozza, G. Costigan, S. Cowell, F. Crifo, M. Crosta, C. Crowley, J. Cuypers, C. Dafonte, Y. Damerdji, A. Dapergolas, M. David, P. de Laverny, F. De Luise, R. De March, R. de Souza, A. de Torres, J. Debosscher, E. del Pozo, A. Delgado, H. E. Delgado, S. Diakite, C. Diener, E. Distefano, C. Dolding, P. Drazinos, J. Durán, B. Edvardsson, H. Enke, K. Eriksson, P. Esquej, G. Eynard Bontemps, C. Fabre, M. Fabrizio, S. Faigler, A. J. Falcão, M. Farràs Casas, L. Federici, G. Fedorets, P. Fernique, F. Figueras, F. Filippi, K. Findeisen, A. Fonti, E. Fraile, M. Fraser, M. Gai, S. Galleti, D. Garabato, F. García-Sedano, A. Garofalo, N. Garralda, A. Gavel, P. Gavras, J. Gerssen, R. Geyer, P. Giacobbe, G. Gilmore, S. Girona, G. Giuffrida, F. Glass, M. Gomes, A. Gueguen, A. Guerrier, R. Gutié, R. Haigron, D. Hatzidimitriou, M. Hauser, M. Haywood, U. Heiter, A. Helmi, J. Heu, T. Hilger, D. Hobbs, W. Hofmann, G. Holland , H. E. Huckle, A. Hypki, V. Icardi, K. Janßen, G. Jevardat de Fombelle, P. G. Jonker, Á. L. Juhász, F. Julbe, A. Karampelas, A. Kewley, J. Klar, A. Kochoska, R. Kohley, K. Kolenberg, M. Kontizas, E. Kontizas, S. E. Koposov, G. Kordopatis, Z. Kostrzewa-Rutkowska, P. Koubsky, S. Lambert, A. F. Lanza, Y. Lasne, J. B. Lavigne, Y. Le Fustec, C. Le Poncin-Lafitte, Y. Lebreton, S. Leccia, N. Leclerc, I. Lecoeur-Taibi, H. Lenhardt, F. Leroux, S. Liao, E. Licata, H. E. P. Lindstrøm, T. A. Lister, E. Livanou, A. Lobel, M. López, S. Managau, R. G. Mann, G. Mantelet, O. Marchal, J. M. Marchant, M. Marconi, S. Marinoni, G. Marschalkó, D. J. Marshall, M. Martino, G. Marton, N. Mary, D. Massari, G. Matijevič, T. Mazeh, P. J. McMillan, S. Messina, D. Michalik, N. R. Millar, D. Molina, R. Molinaro, L. Molnár, P. Montegriffo, R. Mor, R. Morbidelli, T. Morel, D. Morris, A. F. Mulone, T. Muraveva, I. Musella, G. Nelemans, L. Nicastro, L. Noval, W. O'Mullane, D. Ordóñez-Blanco, P. Osborne, C. Pagani, I. Pagano, F. Pailler, H. Palacin, L. Palaversa, A. Panahi, M. Pawlak, A. M. Piersimoni, F. X. Pineau, E. Plachy, G. Plum, E. Poggio, A. Prša, L. Pulone, E. Racero, S. Ragaini, N. Rambaux, M. Ramos-Lerate, S. Regibo, C. Reylé, F. Riclet, V. Ripepi, A. Riva, A. Rivard, G. Rixon, T. Roegiers, M. Roelens, M. Romero-Gómez, N. Rowell, F. Royer, L. Ruiz-Dern, G. Sadowski, T. Sagristà Sellés, J. Sahlmann, J. Salgado, E. Salguero, N. Sanna, T. Santana-Ros, M. Sarasso, H. Savietto, M. Schultheis, E. Sciacca, M. Segol, J. C. Segovia, D. Ségransan, I. C. Shih, L. Siltala, A. F. Silva, R. L. Smart, K. W. Smith, E. Solano, F. Solitro, R. Sordo, S. Soria Nieto, J. Souchay, A. Spagna, U. Stampa, I. A. Steele, H. Steidelmüller, C. A. Stephenson, H. Stoev, F. F. Suess, J. Surdej, L. Szabados, E. Szegedi-Elek, D. Tapiador, F. Taris, G. Tauran, M. B. Taylor, R. Teixeira, D. Terrett, P. Teyssand ier, A. Titarenko, F. Torra Clotet, C. Turon, A. Ulla, E. Utrilla, S. Uzzi, M. Vaillant, G. Valentini, V. Valette, A. van Elteren, E. Van Hemelryck, M. van Leeuwen, M. Vaschetto, A. Vecchiato, J. Veljanoski, Y. Viala, D. Vicente, S. Vogt, C. von Essen, H. Voss, V. Votruba, S. Voutsinas, M. Weiler, O. Wertz, T. Wevers, . Wyrzykowski, A. Yoldas, M. Žerjal, H. Ziaeepour, J. Zorec, S. Zschocke, S. Zucker, C. Zurbach, and T. Zwitter. Gaia Data Release 2. Observations of solar system objects. A&A, 616:A13, Aug 2018.

[10] L. Iess, W. M. Folkner, D. Durante, M. Parisi, Y. Kaspi, E. Galanti, T. Guillot, W. B. Hubbard, D. J. Stevenson, J. D. Anderson, D. R. Buccino, L. Gomez Casajus, A. Milani, R. Park, P. Racioppa, D. Serra, P. Tortora, M. Zannoni, H. Cao, R. Helled, J. I. Lunine, Y. Miguel,

B. Militzer, S. Wahl, J. E. P. Connerney, S. M. Levin, and S. J. Bolton. Measurement of jupiter's asymmetric gravity field. Nature, 555:220 EP –, 03 2018.

[11] L. Iess, B. Militzer, Y. Kaspi, P. Nicholson, D. Durante, P. Racioppa, A. Anabtawi, E. Galanti, W. Hubbard, M. J. Mariani, P. Tortora, S. Wahl, and M. Zannoni. Measurement and implications of saturn's gravity field and ring mass. Science, 364(6445), 2019.

[12] P. Kuchynka and W. M. Folkner. A new approach to determining asteroid masses from planetary range measurements. Icarus, 222:243–253, January 2013.

[13] C. Lawson and R. Hanson. Solving least squares problems. SIAM, 1974.

[14] Hervé Manche. PhD thesis.

[15] Dmitry A. Pavlov, James G. Williams, and Vladimir V. Suvorkin. Determining parameters of Moon's orbital and rotational motion from LLR observations using GRAIL and IERS-recommended models. Celestial Mechanics and Dynamical Astronomy, 126(1-3):61–88, 2016.

[16] G Petit and B Luzum. IERS Conventions (2010). IERS Technical Note, 36, 2010.

[17] E. V. Pitjeva and N. P. Pitjev. Mass of the Kuiper belt. Celestial Mechanics and Dynamical Astronomy, 130(9):57, Sep 2018.

[18] N. Rambaux and J. G. Williams. The Moon's physical librations and determination of their free modes. Celestial Mechanics and Dynamical Astronomy, 109(1):85–100, jan 2011.

[19] V. Viswanathan, A. Fienga, M. Gastineau, and J. Laskar. INPOP17a planetary ephemerides. Notes Scientifiques et Techniques de l'Institut de Mecanique Celeste, 108, August 2017.

[20] V. Viswanathan, A. Fienga, O. Minazzoli, L. Bernus, J. Laskar, and M. Gastineau. The new lunar ephemeris INPOP17a and its application to fundamental physics. Monthly Notices of the Royal Astronomical Society, 476(2):1877–1888, may 2018.

[21] V. Viswanathan, N. Rambaux, A. Fienga, J. Laskar, and M. Gastineau. Observational Constraint on the Radius and Oblateness of the Lunar Core-Mantle Boundary. Geophysical Research Letters, 46(13):7295–7303, jul 2019.

[22] Vishnu Viswanathan. Improving the dynamical model of the Moon using lunar laser ranging and spacecraft data. Phd thesis, Observatoire de Paris, 2017.

[23] Vishnu Viswanathan, Erwan Mazarico, Sander J Goossens, and Stefano Bertone. On the grail-llr low-degree gravity field inconsistencies. In AGU Fall Meeting 2019. AGU, 2019.

[24] James G. Williams and Dale. H. Boggs. Tides on the Moon: Theory and determination of dissipation. Journal of Geophysical Research: Planets, 120(4):689–724, apr 2015.

[25] James G. Williams, Dale. H. Boggs, and William M. Folkner. DE430 Lunar Orbit, Physical Librations, and Surface Coordinates. Technical report, JPL, Caltech, 2013.

8 Annex

Table 10: Asteroid masses (GM).

IAU	GM $10^{18}AU^3.d^{-2}$	1-σ $10^{18}AU^3.d^{-2}$	IAU	GM $10^{18}AU^3.d^{-2}$	1-σ $10^{18}AU^3.d^{-2}$
1	139643.532	340.331	233	316.961	140.441
2	32613.272	183.269	236	190.650	88.318
3	3806.229	126.860	238	559.720	233.434
4	38547.977	93.970	240	85.484	40.914
5	465.987	46.044	241	963.174	342.190
6	986.372	120.710	247	105.893	51.632
7	1833.933	84.518	250	245.307	120.373
8	596.962	62.983	259	808.064	296.308
9	1215.881	132.841	266	248.112	117.623
10	11954.671	449.263	268	134.613	65.831
11	977.184	157.265	275	233.252	110.230
12	229.191	45.153	276	452.566	217.572
13	546.734	173.058	283	237.643	112.678
14	765.291	117.763	287	33.835	16.849
15	3936.840	226.670	303	80.021	39.909
16	3088.668	323.861	304	14.118	7.043
17	118.120	55.782	308	289.006	137.485
18	576.019	48.935	313	72.947	30.632
19	1231.401	72.659	322	36.047	17.925
20	254.982	101.997	324	1682.131	45.327
21	257.961	96.045	326	45.434	21.252
22	1043.715	323.477	328	323.707	152.584
23	338.255	62.375	329	46.065	22.861
24	554.975	233.558	334	572.159	232.556
25	159.836	67.413	335	73.943	34.109
26	94.632	46.747	336	64.361	29.608
27	646.483	132.326	337	87.950	40.988
28	643.077	167.700	338	22.106	11.047
29	2103.023	187.853	344	372.187	75.866
30	238.456	96.799	345	100.699	48.761
31	1268.115	412.584	346	140.482	69.103
32	106.167	49.620	347	30.486	15.095
34	291.626	134.149	349	276.607	130.263
35	166.718	76.290	350	253.986	125.400
36	245.514	86.582	354	1078.281	183.015
37	189.707	84.623	356	108.613	50.163
38	49.830	24.817	357	131.750	65.607
39	939.076	279.684	358	61.697	30.742
40	350.481	89.957	360	436.211	189.055
41	723.534	121.258	362	76.350	37.995
42	147.445	47.113	363	207.657	98.134
43	74.755	25.136	365	76.459	37.909
44	68.184	33.458	366	114.144	56.805
45	1115.547	275.717	369	48.370	24.090

Continued on next page

Table 10 – *Continued from previous page*

IAU	GM $10^{18}AU^3.d^{-2}$	1-σ $10^{18}AU^3.d^{-2}$	IAU	GM $10^{18}AU^3.d^{-2}$	1-σ $10^{18}AU^3.d^{-2}$
46	135.706	62.782	372	1237.702	324.096
47	144.403	70.451	373	76.503	38.097
48	1318.034	512.014	375	465.838	214.300
49	176.639	85.388	377	38.443	19.191
50	124.107	42.027	381	495.946	217.389
51	417.753	140.463	385	111.656	54.700
52	2308.950	420.581	386	550.244	212.234
53	128.326	56.579	387	132.193	60.346
54	371.895	141.535	388	215.378	105.901
56	797.238	96.698	389	104.021	50.336
57	454.114	203.249	393	285.309	91.258
58	44.048	21.967	404	89.289	41.338
59	473.769	190.829	405	240.229	51.530
60	12.497	6.185	407	101.937	50.366
62	43.570	21.758	409	1011.800	201.135
63	150.988	66.373	410	303.222	96.475
65	2990.906	504.055	412	166.019	80.653
68	321.421	135.243	415	99.281	46.367
69	595.357	206.760	416	123.889	59.146
70	213.930	92.797	419	255.322	72.371
71	97.797	48.104	420	220.068	108.699
72	82.722	37.582	423	654.344	264.106
74	101.895	48.951	424	67.947	33.820
75	71.329	31.690	426	228.829	109.764
76	482.278	201.446	431	107.679	53.226
77	31.841	15.873	432	15.057	7.483
78	444.357	84.087	433	3.548	1.037
79	44.034	21.633	442	24.960	12.436
80	89.737	38.401	444	889.725	221.210
81	200.226	91.279	445	47.050	23.497
82	36.088	17.982	449	17.583	8.776
83	93.231	45.344	451	1671.212	588.194
84	45.404	19.210	454	21.631	10.802
85	884.824	146.811	455	340.048	111.366
86	247.214	118.942	464	125.102	60.637
87	2726.311	531.952	465	24.069	12.025
88	0.055	0.027	466	91.237	45.521
89	557.072	133.009	469	304.433	137.562
90	146.728	72.165	471	528.244	191.253
91	100.804	48.968	476	342.566	148.598
92	375.176	176.150	481	64.673	32.135
93	350.267	145.906	485	22.236	11.103
94	713.723	313.444	488	561.612	229.459
95	151.282	75.253	489	121.924	60.490
96	431.057	177.179	490	69.112	34.496

Continued on next page

Table 10 – *Continued from previous page*

IAU	GM $10^{18}AU^3.d^{-2}$	1-σ $10^{18}AU^3.d^{-2}$	IAU	GM $10^{18}AU^3.d^{-2}$	1-σ $10^{18}AU^3.d^{-2}$
97	210.124	78.474	491	202.066	99.899
98	129.270	59.993	498	91.707	44.284
99	75.571	35.518	503	45.347	22.078
100	124.982	61.740	505	166.145	69.346
102	236.332	88.196	506	322.294	155.267
103	151.309	74.011	508	206.435	102.288
104	163.453	80.618	511	6637.430	481.733
105	171.787	69.850	514	219.734	107.830
106	337.535	159.721	516	52.638	24.191
107	1422.992	464.415	517	100.264	49.805
109	51.619	24.915	521	76.898	37.306
110	127.185	62.490	532	1213.536	151.443
111	108.247	51.280	535	23.438	11.701
112	47.020	23.052	536	808.338	364.913
113	21.370	10.651	545	170.952	83.798
114	131.966	62.975	547	21.620	10.793
115	47.322	23.309	554	126.682	60.162
117	1453.566	435.368	566	541.209	240.020
118	9.548	4.771	568	50.683	25.276
120	502.516	232.707	569	43.667	21.659
121	713.675	291.224	584	20.399	10.034
124	166.505	76.974	585	5.529	2.876
127	117.181	57.880	591	30.558	15.074
128	618.626	210.888	593	62.446	30.550
129	684.256	200.467	595	93.310	46.541
130	864.951	294.577	596	178.840	85.354
132	30.303	14.755	598	20.551	10.265
134	173.804	78.883	599	71.685	34.736
135	136.653	59.914	602	168.836	82.134
137	277.249	126.850	604	53.701	26.742
139	404.038	108.798	618	166.141	82.396
140	360.331	130.179	623	7.431	3.713
141	115.238	54.453	626	72.832	35.212
143	51.644	25.749	635	57.819	28.865
144	471.278	121.876	654	188.097	56.725
145	461.851	123.055	663	239.643	114.428
146	209.047	101.392	667	73.041	36.352
147	78.621	39.220	674	193.640	91.865
148	129.656	63.668	675	96.325	46.769
150	106.505	52.648	680	206.775	96.732
154	817.895	322.045	683	295.566	141.445
156	429.780	81.628	690	201.167	98.318
159	270.009	131.608	691	92.304	45.887
160	89.965	44.536	694	153.259	56.940
162	203.147	92.477	696	99.448	49.299

Continued on next page

Table 10 – *Continued from previous page*

IAU	GM $10^{18}AU^3.d^{-2}$	1-σ $10^{18}AU^3.d^{-2}$	IAU	GM $10^{18}AU^3.d^{-2}$	1-σ $10^{18}AU^3.d^{-2}$
163	21.516	10.609	702	906.957	374.186
164	470.318	107.979	704	4737.367	426.508
165	285.680	139.537	705	324.182	154.286
168	444.827	206.958	709	292.189	137.624
171	139.839	69.453	712	365.024	119.975
172	79.253	38.036	713	111.487	55.303
173	306.789	136.442	735	38.073	18.737
175	142.881	70.244	739	184.532	84.457
176	144.007	71.451	740	177.118	86.570
177	28.753	14.306	747	801.111	138.793
181	439.780	193.506	751	113.875	53.535
185	774.136	243.015	752	26.569	13.253
187	372.900	86.373	760	66.464	32.580
191	93.987	46.655	762	134.105	66.593
192	230.535	70.417	769	94.090	46.690
194	523.744	107.014	772	61.622	30.734
195	69.927	34.800	773	68.306	34.041
196	867.047	361.097	776	398.260	174.681
198	29.651	14.406	778	21.890	10.936
200	266.130	125.838	780	208.182	102.535
201	176.335	84.064	784	36.056	17.994
203	169.328	82.667	786	237.241	112.327
205	14.818	7.408	788	235.031	115.048
206	207.589	100.326	790	537.375	257.943
209	180.181	89.822	791	87.213	43.342
210	22.894	11.438	804	651.926	227.504
211	275.891	133.146	814	186.167	88.930
212	133.713	66.259	849	130.090	64.042
213	40.499	20.206	895	203.534	100.739
216	687.345	173.442	909	361.354	173.346
221	155.795	76.814	914	53.687	26.163
223	88.982	44.217	980	73.406	36.296
224	64.429	31.805	1015	39.901	19.940
225	121.946	60.326	1021	138.012	62.136
227	233.312	109.782	1036	9.792	4.344
230	349.702	141.842	1093	134.311	65.664
			1107	165.609	83.314
			1171	84.409	41.675
			1467	51.282	27.305